

## Petrography and geochemistry of accreted oceanic fragments below the Western Cordillera of Ecuador

ANDREA AMÓRTEGUI,<sup>1\*</sup> ETIENNE JAILLARD,<sup>1</sup> HENRIETTE LAPIERRE,<sup>1†</sup> JEAN-EMMANUEL MARTELAT,<sup>1</sup> DELPHINE BOSCH<sup>2</sup> and FRANCOIS BUSSY<sup>3</sup>

<sup>1</sup>Université de Grenoble (UJF), LGCA, UMR 5025, Maison des Géosciences, BP 53, 38041 Grenoble Cedex 09, France

<sup>2</sup>Géosciences Montpellier, UMR-CNRS 5243, Institut des Sciences de la Terre, de l'Eau et de l'Espace de Montpellier, Place Eugène Bataillon, 34095, France

<sup>3</sup>University of Lausanne, Institute of Mineralogy and Geochemistry, BSFH-2, CH-1015 Lausanne, France

(Received October 26, 2009; Accepted June 10, 2010)

The Western Cordillera of Ecuador consists of Cretaceous crustal fragments of oceanic plateaus and superimposed insular arcs, which were accreted to the northwestern South American margin during the Late Cretaceous and Paleocene. Slices of high-grade metabasites, ultramafic rocks, gabbros and basalts, unmetamorphosed radiolarian cherts and scarce garnet-bearing metasediments were randomly exhumed along Miocene to Recent transcurrent faults crosscutting the Western Cordillera. The basalts show geochemical characteristics of oceanic plateau basalts (flat REE patterns, La/Nb = 0.85). The gabbros differ from the basalts in having lower REE levels, positive Eu anomalies, and negative Nb and Ta anomalies; they are interpreted as resulting from arc magmatism. The amphibolites and banded amphibolites have major and trace element chemistry similar to that of oceanic plateau basalts (flat REE patterns, La/Nb = 0.86) or to cumulate gabbros. The granulite shares with oceanic plateaus similar trace element chemistry (flat REE patterns, La/Nb < 1) and  $\epsilon_{\text{Nd}_i}$  values (+7.6). Continent-derived metasediments are depleted in heavy REE (La/Y = 4.8) and have a negative Eu anomaly. Foliated lherzolites, melagabbronorites and pyroxenites consist of serpentinized olivine + cpx + opx  $\pm$  Ca-plagioclase. Lherzolites, melagabbronorites and pyroxenites are LREE depleted with positive Eu anomalies, while the harzburgite displays a U-shaped REE pattern. The trace element abundances of the ultramafic rocks are very low (0.1 to 1 times the chondritic and primitive mantle values). The ultramafic rocks represent fragments of depleted mantle, deformed cpx-rich cumulate, and continental lithospheric mantle or mantle contaminated by subduction-fluid. Except the scarce quartz-rich metasediments, all these rocks likely represent remnants of accreted oceanic crustal fragments and associated depleted mantle. Since these samples were randomly sampled at depth by the fault, we propose that the Western Cordillera and its crustal root are mainly of oceanic nature.

Keywords: Ecuador, Western Cordillera, accreted oceanic terranes, exhumation

### INTRODUCTION

The build-up of the Andean belt is linked to subduction of the Pacific lithosphere beneath the South American plate (Gansser, 1973; Dewey and Lamb, 1992; Jaillard *et al.*, 2000). However, the processes of the Andean orogeny change with latitude along the range. In the central Andes, continental crust shortening predominates (Suarez *et al.*, 1983; Baby *et al.*, 1997; Müller *et al.*, 2002), whereas accretion and underplating of exotic oceanic terranes occurred in the north (Gansser, 1973;

Reynaud *et al.*, 1999; Mamberti *et al.*, 2004; Kerr *et al.*, 1997), and likely contributed to the formation of the crustal root of the northern Andes (Guillier *et al.*, 2001; Jaillard *et al.*, 2000, 2002). Several crustal fragments of oceanic plateaus overlain by island arcs were accreted to the active margin of Ecuador between ~80 and 40 Ma and presently crop out in the Western Cordillera (Reynaud *et al.*, 1999; Lapierre *et al.*, 2000; Kerr *et al.*, 1997, 2002; Allibon *et al.*, 2008). Later, dextral, transpressive faults (McCourt *et al.*, 1998; Hughes and Pilatasig, 2002; Jaillard *et al.*, 2004) affected the pile of accreted oceanic terranes, resulting in the exhumation of varied metamorphic or non-metamorphosed oceanic rocks. The aim of this work is to present the results of petrographical, mineralogical, geochemical and isotopical analysis of these granulites, amphibolites, banded amphibolites, micaschists, peridotites and pyroxenites. For this study, samples of these rocks were collected along three sec-

\*Corresponding author (e-mail: amortegui\_vera.a\_ekaterina@uqam.ca)

\*Present address: Université du Québec à Montréal, Département des Sciences de la Terre et de l'Atmosphère, Montréal, QC, Canada.

†Deceased in January 2006.

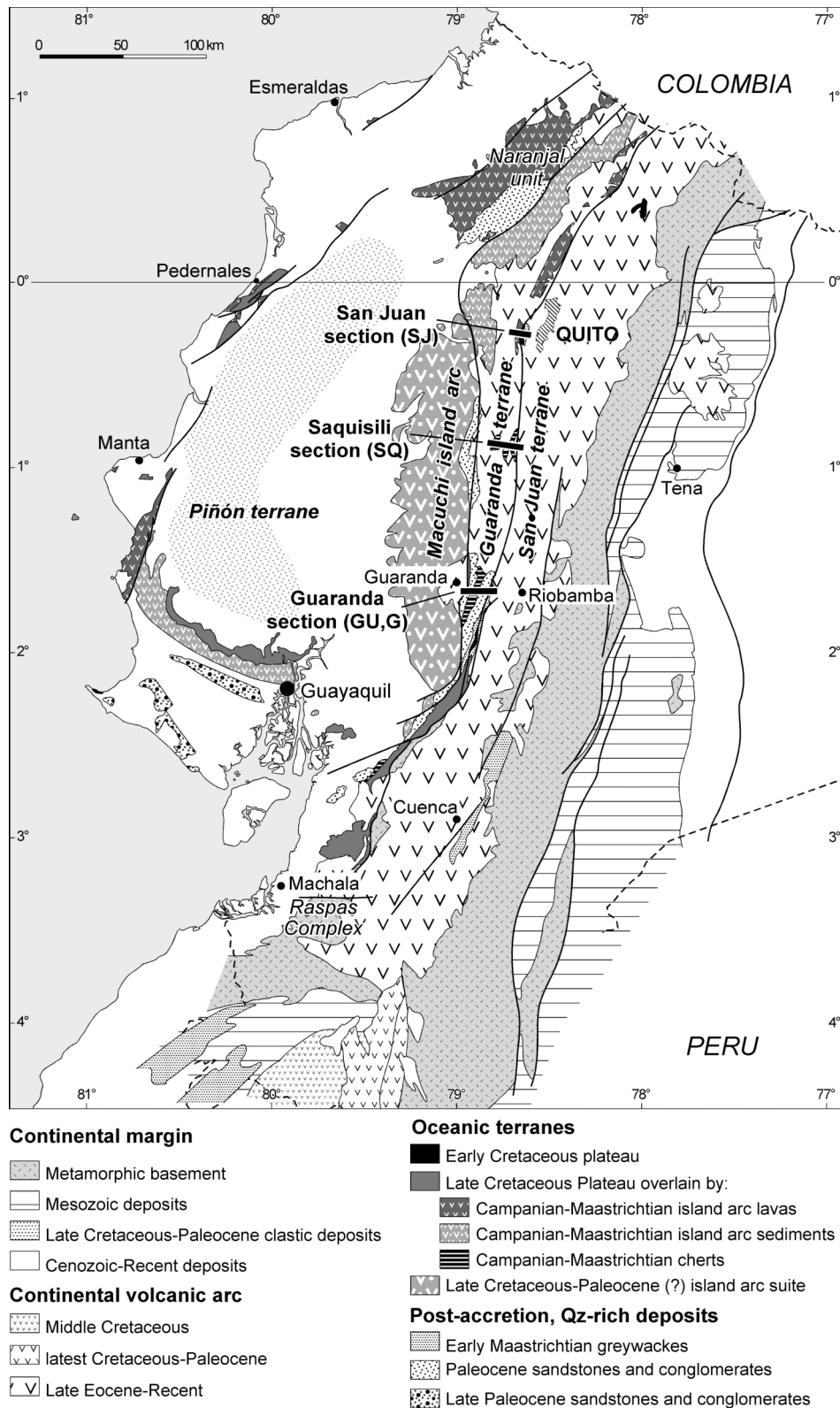


Fig. 1. Simplified geological map of Ecuador (from Jaillard et al., 2009). Different accretions episodes occurred in Late Cretaceous in the Andes Cordillera. The map shows three studied sections: San Juan (SJ), Saquisilí (SQ) and Guaranda (GU, G).

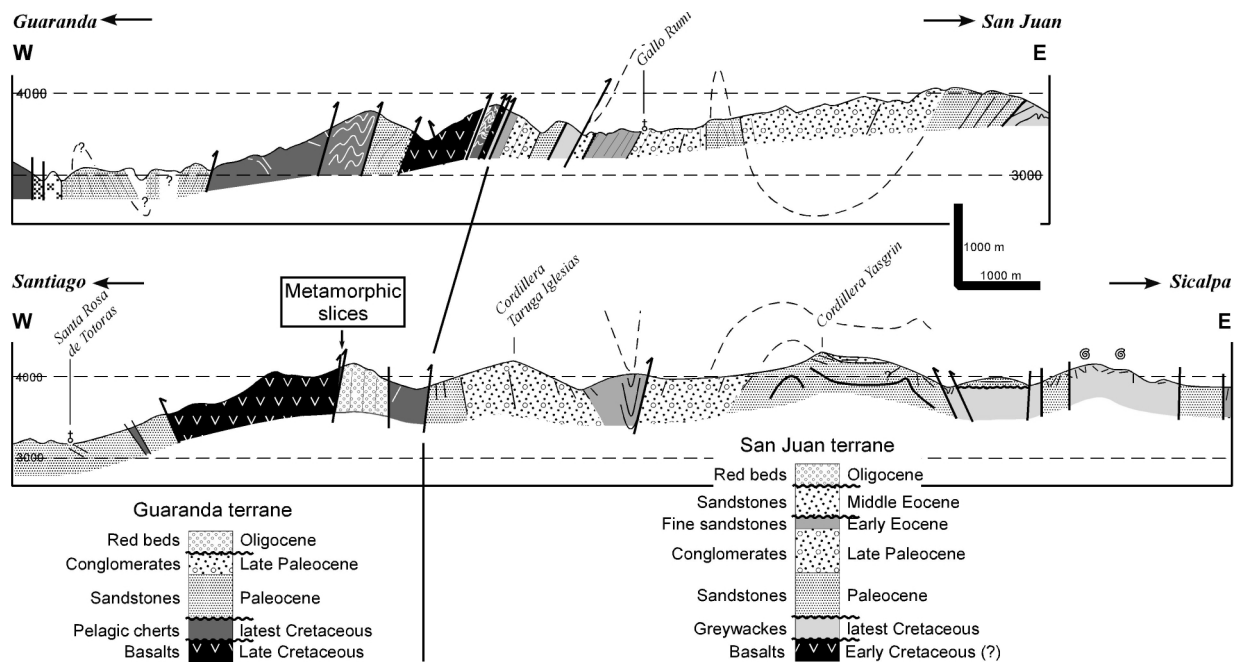


Fig. 2. Cross sections of the Western Cordillera, West of Riobamba (Guaranda section, Fig. 1). The sections show that different multi-kilometre scale strike slip faults affected the accreted oceanic terrains and triggered the formation of flower structures in the Western Cordillera (simplified after Jaillard *et al.*, 2004).

tions of the Western Cordillera, West of Quito (samples SJ), West of Saquisilí (samples SQ) and West of Riobamba (samples GU and G; Fig. 1), and twenty-six out of them were analyzed with the aim of understanding the origin and evolution of these exhumed rocks.

### GEOLOGICAL SETTING

Ecuador comprises six different morphological domains. From east to west these are the Oriente basin, the Subandean Zone, the Eastern Cordillera, the Interandean Valley, the Western Cordillera, and the Coastal Zone (Fig. 1). The Oriente basin represents the present-day eastern foreland basin of the Andean orogen (Litherland *et al.*, 1993; Jaillard *et al.*, 1997; Ruiz *et al.*, 2004). The Ecuadorian Andes are formed by the Eastern and Western Cordilleras, which are separated by the Interandean Valley. The Eastern Cordillera consists of deformed Paleozoic to Mesozoic metamorphic rocks (Aspden and Litherland, 1992; Litherland *et al.*, 1994), while the Western Cordillera is composed of oceanic terranes accreted to the Andean margin between the Late Campanian and the Palaeocene (Cosma *et al.*, 1998; Reynaud *et al.*, 1999; Hughes and Pilatasig, 2002; Kerr *et al.*, 2002; Mamberti *et al.*, 2003, 2004; Jaillard *et al.*, 2009). The Coastal Zone consists of basalts and dolerites of oceanic plateau affinity, overlain by Late Cretaceous island arc-rocks (e.g., Goossens and Rose, 1973; Lebrat *et al.*, 1987; Reynaud

*et al.*, 1999; Luzieux *et al.*, 2006).

Two lithological associations of oceanic plateau affinity characterize the accreted oceanic terranes. Type I association is composed of basaltic and picritic massive and pillow lava flows, tuffs and greywackes, intruded by shallow-level gabbros and dolerites. This type is widely exposed in the Piñón Formation on the coast (Reynaud *et al.*, 1999) and in the Western Cordillera, where it is called the Pallantanga Unit (McCourt *et al.*, 1998; Kerr *et al.*, 2002; Hughes and Pilatasig, 2002; Mamberti *et al.*, 2003). On the basis of paleontological and radiometric data (Luzieux *et al.*, 2006; Vanmelle *et al.*, 2008), Type I is regarded as belonging to the Cretaceous Caribbean Colombian oceanic plateau (CCOP; Kerr *et al.*, 1997).

Type II lithological association consists of cumulate peridotites and gabbros intruded by mafic and felsic dykes (Mamberti *et al.*, 2004). This type occurs as tectonic slices within the Late Cretaceous suture, east of the Western Cordillera. It is dated, either as early Cretaceous ( $123 \pm 13$  Ma, isochron plot for minerals and whole-rock, Lapiere *et al.*, 2000), or as Late Cretaceous ( $87.10 \pm 1.66$  Ma, U–Pb zircon age, Vallejo *et al.*, 2006). Whatever the case, this “San Juan” oceanic terrane accreted to the Ecuadorian margin prior to the Pallantanga and Piñón terranes (Jaillard *et al.*, 2004, 2009).

Island arc rocks are also exposed in the Western Cordillera and in coastal Ecuador. These arc fragments rest on Late Cretaceous oceanic plateau rocks, are Late

Table 1. Petrographic features of the studied samples

	Texture	Minerals	Rock type
<b>Igneous rocks</b>			
02SQ3	Porphyritic	Pl + Cpx (+ Opx)	Basalt
03GU12	Porphyritic	Pl + Cpx	Basalt
02GU10	Ophitic	Pl + Cpx	Dolerite
02GU11A	Ophitic	Pl + Cpx	Dolerite
02GU16	Ophitic	Pl + Cpx	Dolerite
02GU12A	Mesocumulate	} Pl (35–40%) + Opx (15–25%) + Cpx (25%) + amphibole (15%) + Fe–Ti oxides (4%)	Gabbro
02GU8A	Magmatic layering		Gabbro (altered)
03G21	Mesocumulate, layered		Gabbro
<b>Metamorphic rocks</b>			
02GU12	Weak foliation	Opx + Cpx + Pl + Qz	Granulite
02GU6	Heterobl. nematobl., layered	Mg–Hb (40–50%)	Amphibolite
03G23	Foliated	+Cpx (10–30%)	Amphibolite
04SQ3	Foliated	+Pl (15–52%)	Amphibolite
03SQ9	Foliated	+Oxides (1%) + Sphene	Amphibolite
04GU8	Granoblastic, foliated	Hb (60%) + Pl (40%)	Banded amphibolite
04GU12	Porphyrobl. granobl., foliated	Pl (60%) + Hb (35%) + Actinolite	Banded amphibolite
03G22B	Granoblastic, foliated	Amph (50%) + Pl (48%)	Banded amphibolite
04SJ1	Foliated	Pheng, W-Mica, Garnet, Epid (15%), Graphite	Micaschist
04SJ6	Foliated	Pheng, W-Mica, Chltoi, Epid, Graphite (50%)	Micaschist
<b>Melagabbroonorites and Ultramafic rocks</b>			
03SJ4	Adcumulate	Cpx (75%) + Pl (25%)	Melagabbroonorite
03G18	Adcumulate	Cpx + Opx + Pl	Melagabbroonorite
03SJ3	Cumulate	Cpx (65%) + Pl (25%) + Ol (10%)	Melagabbroonorite
03SQ22	Foliated	Cpx + Opx + green spinel	Pyroxenite
04SQ11	Foliated	Cpx (52%), Opx (38%), Pl, spinel, serpent. Ol	Pyroxenite
03SJ2	Foliated	Ol (35%), Cpx (30%), Opx (20%), Pl (15%)	Lherzolite
03SQ18	Blastomylonitic, foliated	Ol (85%), Opx (7%), green spinel (5%)	Lherzolite
98SQ3	Intensely foliated	Ol (84%), Opx (8%), Cpx (5%), picotite (3%)	Harzburgite

Cretaceous in age, and accreted to the Pacific margin of Ecuador during the latest Cretaceous–Paleogene (Jaillard *et al.*, 2004, 2009; Luzieux *et al.*, 2006; Vallejo *et al.*, 2006).

After accretion of the oceanic terranes, subduction of the Pacific plate resumed, and an Andean-type magmatic arc developed in the late Eocene–Oligocene first in the Western Cordillera (Kehrer and van der Kaaden, 1979; Egüez, 1986) and then migrated to the east (Barragán *et al.*, 1998; Bourdon *et al.*, 2003). Since the Eocene, dextral, transpressive, multi kilometer-scale strike-slip faults affected the accreted oceanic terranes, triggering the formation of flower structures in the Western Cordillera (Fig. 2; McCourt *et al.*, 1998; Jaillard *et al.*, 2004). In the study area, N- to NNE-trending strike-slip faults crosscut

Oligocene deposits, and are offset by NE-trending dextral faults, which also crosscut Late Miocene volcanic units. These Miocene faults exhumed various slices of radiolarian cherts, metamorphic rocks (amphibolites, granulites, amphibolitic gneisses, micaschists), magmatic rocks (basalts, dolerites, gabbros), and cumulate and foliated ultramafic rocks (lherzolites, harzburgites and pyroxenites).

#### ANALYTICAL PROCEDURES

Major and compatible trace elements were determined by ICP-optical emission spectroscopy at the Centre de Recherches Pétrographiques et Géochimiques in Nancy and at the Université de Bretagne Occidentale in Brest,

Table 2. Major and trace elements of igneous rocks

Rock type Sample No.	Basalt 02SQ3	Basalt 03G12	Dolerite 02GU10	Dolerite 02GU11A	Dolerite 02GU16	Gabbro 02GU12A	Gabbro 02GU8A	Gabbro 03G21
SiO <sub>2</sub> [%]	60.90	62.10	46.51	54.02	51.54	49.21	49.88	45.64
Al <sub>2</sub> O <sub>3</sub>	15.85	15.85	14.32	11.19	13.56	12.32	12.49	48.55
Fe <sub>2</sub> O <sub>3</sub>	5.85	5.85	13.09	9.74	10.38	9.39	9.52	15.10
MnO	0.11	0.11	0.26	0.18	0.17	0.19	0.19	9.94
MgO	3.71	3.71	9.64	6.72	7.85	13.95	14.14	0.28
CaO	6.43	6.43	10.92	12.20	11.06	12.36	12.53	19.12
Na <sub>2</sub> O	3.29	3.29	2.36	2.92	2.15	1.04	1.05	4.68
K <sub>2</sub> O	1.20	1.20	0.13	0.03	0.33	0.00	0.00	0.66
TiO <sub>2</sub>	0.72	0.72	1.32	1.07	0.95	0.19	0.19	1.36
P <sub>2</sub> O <sub>5</sub>	<dl	n.a.	<dl	n.a.	n.a.	<dl	<dl	0.06
LOI	1.95	0.14	1.45	1.92	2.00	1.70	1.70	<dl
Total	100.01	99.83	100.00	99.99	99.99	100.35	99.84	1.90
Th [ppm]	2.798	0.401	0.278	0.333	0.213	0.005	0.047	0.008
U	0.892	0.120	0.077	0.095	0.069	0.001	0.026	0.000
Nb	4.732	4.910	4.400	5.419	3.377	0.027	0.471	0.028
Ta	0.303	0.309	0.280	0.337	0.213	0.003	0.017	0.002
La	12.545	4.194	3.392	3.863	2.672	0.277	1.040	1.669
Ce	25.634	10.727	9.361	10.021	7.229	0.740	2.831	3.508
Pb	6.409	0.580	1.026	0.922	0.186	0.367	0.275	0.140
Pr	3.501	1.541	1.531	1.521	1.144	0.141	0.418	0.854
Sr	655.310	67.376	89.931	658.784	107.157	71.690	110.071	68.927
Nd	14.284	7.535	7.855	7.458	6.043	0.864	1.864	4.724
Zr	101.840	69.997	25.775	55.235	54.481	2.846	n.a.	n.a.
Hf	2.563	1.846	1.084	1.538	1.472	0.116	n.a.	n.a.
Sm	3.095	2.546	2.699	2.192	2.062	0.385	0.225	0.068
Eu	0.937	0.872	0.964	0.814	0.777	0.235	0.260	0.589
Ti	11625	6967	15219	14574	12271	1156	360	735
Gd	2.901	3.226	3.666	2.611	2.829	0.694	0.472	2.086
Tb	0.409	0.605	0.671	0.433	0.516	0.134	0.085	0.347
Dy	2.239	3.982	4.305	2.564	3.392	0.965	0.515	2.243
Y	12.894	24.993	27.494	14.832	22.112	5.884	3.497	4.323
Ho	0.449	0.840	0.908	0.537	0.746	0.228	0.115	0.496
Yb	1.114	2.514	2.485	1.157	2.066	0.672	0.384	1.301
Er	1.232	2.521	2.649	1.428	2.139	0.671	0.344	1.485
Lu	0.166	0.403	0.381	0.179	0.324	0.107	0.074	0.195
La/Yb	11.300	1.670	1.360	3.340	1.290	0.412	2.710	1.280
La/Nb	2.650	0.854	0.771	0.713	0.791	10.270	2.210	60.700

<dl: below detection limit.

n.a.: no available.

Table 3. Major and trace elements of metamorphic rocks

Rock type Sample No.	Granul 02GUT2	Amph 02GU6	Amph 03G23	Amph 04SQ3	Amph 03SQ9	B-amph 04GU8	B-amph 04GU12	B-amph 03G22B	M-schist 04SJ1	M-schist 04SJ6						
SiO <sub>2</sub> [%]	49.43	50.74	46.30	47.60	57.00	58.40	45.00	47.50	46.80	47.80	49.00	50.10	61.00	63.00	Dry	75.60
Al <sub>2</sub> O <sub>3</sub>	12.89	13.23	13.90	14.30	14.80	15.10	16.20	17.10	16.20	16.60	13.10	13.30	16.00	16.50	16.30	16.30
Fe <sub>2</sub> O <sub>3</sub>	12.19	12.51	9.80	10.10	6.60	6.70	12.40	13.10	9.80	11.20	8.90	9.10	6.70	6.90	2.20	2.30
MnO	0.25	0.26	0.30	0.20	0.10	0.10	0.20	0.20	0.20	0.20	0.20	0.20	0.20	0.20	0.00	0.00
MgO	9.96	10.22	10.00	10.20	14.40	6.10	8.50	9.00	11.10	11.30	13.00	13.30	3.20	3.30	0.60	0.60
CaO	9.44	9.69	9.40	9.70	11.10	11.40	7.50	7.70	10.20	10.50	12.50	12.80	3.80	3.90	0.20	0.20
Na <sub>2</sub> O	1.98	2.03	2.00	2.00	4.10	4.20	1.70	1.80	1.10	1.10	0.80	0.80	3.50	3.70	1.10	1.10
K <sub>2</sub> O	0.11	0.11	0.10	0.10	0.40	0.40	0.30	0.30	0.20	0.20	0.60	0.60	1.60	1.60	2.70	2.80
TiO <sub>2</sub>	1.17	1.20	0.60	0.60	0.80	0.80	0.60	0.70	0.30	0.30	0.20	0.20	0.60	0.60	1.10	1.10
P <sub>2</sub> O <sub>5</sub>	n.a.	n.a.	0.10	0.10	0.20	0.20	0.10	0.10	<dl	<dl	<dl	<dl	0.20	0.20	<dl	<dl
LOI	2.58	2.60	2.70	2.20	5.30	2.20	5.30	1.40	2.40	2.40	2.20	2.20	3.40	3.40	3.70	3.70
Org. matter	100.00	100.00	99.90	99.80	99.80	99.80	99.80	100.00	100.20	100.20	100.00	100.00	100.10	101.60	101.60	101.60
Th [ppm]	0.005	0.190	0.181	0.031	0.009	0.124	0.006	0.006	0.006	0.006	0.042	0.042	8.900	8.900	6.980	6.980
U	0.003	0.062	0.057	0.012	0.007	0.061	0.005	0.005	0.005	0.005	0.022	0.022	2.560	2.560	2.140	2.140
Nb	1.360	4.146	2.186	0.423	1.019	0.125	0.033	0.033	0.033	0.161	0.161	0.161	3.950	3.950	10.300	10.300
Ta	0.070	0.245	0.126	0.023	0.037	0.010	0.004	0.004	0.004	0.009	0.009	0.009	0.370	0.370	0.850	0.850
La	1.007	3.430	1.869	0.711	0.419	0.509	0.419	0.162	0.162	0.476	0.476	0.476	18.500	18.500	19.100	19.100
Ce	3.139	9.753	4.916	2.430	0.795	1.080	0.127	0.127	0.127	1.109	1.109	1.109	36.900	36.900	30.600	30.600
Pb	0.477	0.352	0.284	0.180	0.195	0.127	0.127	0.127	0.127	0.198	0.198	0.198	30.900	30.900	23.600	23.600
Pr	0.606	1.577	0.695	0.507	0.121	0.149	0.067	0.067	0.067	1.109	1.109	1.109	4.710	4.710	4.390	4.390
Sr	70.382	90.708	77.939	293.000	167.307	58.800	47.700	47.700	47.700	62.379	62.379	62.379	206.000	206.000	86.200	86.200
Nd	3.483	8.003	3.606	3.040	0.626	0.801	0.424	0.424	0.424	19.300	19.300	19.300	16.600	16.600	16.600	16.600
Zr	8.637	23.324	20.411	13.400	15.944	3.420	1.670	1.670	1.670	4.659	4.659	4.659	138.000	138.000	200.000	200.000
Hf	0.324	1.067	0.613	0.546	0.224	0.128	0.058	0.058	0.058	0.147	0.147	0.147	3.830	3.830	5.220	5.220
Sm	1.361	2.681	1.265	0.451	0.594	0.340	0.182	0.182	0.182	0.365	0.365	0.365	4.390	4.390	3.240	3.240
Eu	0.561	0.943	0.451	0.220	0.187	0.210	0.102	0.102	0.102	0.238	0.238	0.238	1.000	1.000	0.762	0.762
Gd	2.045	3.524	1.614	0.620	0.413	0.535	0.316	0.316	0.316	0.585	0.585	0.585	3.910	3.910	2.560	2.560
Tb	0.378	0.638	0.310	0.274	0.070	0.117	0.135	0.135	0.135	0.123	0.123	0.123	0.633	0.633	0.423	0.423
Dy	2.519	4.136	2.037	1.780	0.645	0.835	0.474	0.474	0.474	0.912	0.912	0.912	4.010	4.010	2.600	2.600
Y	15.922	26.239	14.080	11.100	15.029	5.740	3.550	3.550	3.550	6.344	6.344	6.344	23.500	23.500	15.500	15.500
Ho	0.569	0.895	0.433	0.386	0.152	0.203	0.117	0.117	0.117	0.209	0.209	0.209	0.800	0.800	0.529	0.529
Yb	1.590	2.393	1.276	0.925	0.492	0.554	0.397	0.397	0.397	0.662	0.662	0.662	2.650	2.650	1.880	1.880
Er	1.619	2.532	1.240	1.100	0.463	0.600	0.385	0.385	0.385	0.642	0.642	0.642	2.420	2.420	1.660	1.660
Lu	0.253	0.364	0.194	0.144	0.076	0.101	0.065	0.065	0.065	0.107	0.107	0.107	0.427	0.427	0.310	0.310
La/Yb	0.630	1.430	1.460	0.769	0.851	0.919	0.408	0.408	0.408	0.719	0.719	0.719	6.980	6.980	1.230	1.230
La/Nb	0.740	0.827	0.855	1.680	0.411	4.070	4.980	4.980	4.980	2.950	2.950	2.950	4.680	4.680	1.850	1.850

<dl: below detection limit.  
n.a.: no available.

Table 4. Major and trace elements of melagabbronites and ultramafic rocks

Rock type Sample No.	Melagabbron 03S14	Melagabbron 03G18	Melagabbron 03S13	Pyrox 03SQ22	Pyrox 04SQ11	Lherz 03S12	Lherz 03SQ18	Harzb 98SQ3
SiO <sub>2</sub> [%]	49.20	52.60	46.30	44.60	n.a.	44.34	40.24	39.32
Al <sub>2</sub> O <sub>3</sub>	13.40	2.40	4.60	14.10	n.a.	11.58	2.60	0.81
Fe <sub>2</sub> O <sub>3</sub>	3.80	7.70	7.20	4.80	n.a.	6.44	8.01	7.43
MnO	0.10	0.20	0.10	0.10	n.a.	0.10	0.11	0.10
MgO	12.40	18.10	22.70	19.30	n.a.	19.55	35.49	43.06
CaO	19.50	16.20	14.90	14.70	n.a.	13.44	1.56	0.15
Na <sub>2</sub> O	0.70	0.20	0.20	0.50	n.a.	0.41	<dl	<dl
K <sub>2</sub> O	<dl	<dl	<dl	<dl	n.a.	<dl	<dl	<dl
TiO <sub>2</sub>	0.10	0.20	0.10	0.10	n.a.	0.05	<dl	<dl
P <sub>2</sub> O <sub>5</sub>	<dl	<dl	<dl	0.10	n.a.	0.05	<dl	<dl
LOI	1.20	1.90	2.60	1.70	n.a.	3.95	12.15	15.32
Total	100.50	99.40	98.80	100.00		99.91	100.25	99.39
Th [ppm]	0.023	0.024	0.011	0.002	0.006	0.004	0.056	0.004
U	0.005	0.005	<dl	<dl	0.005	0.002	0.251	0.011
Nb	0.026	0.023	0.029	0.012	0.055	0.009	0.057	0.011
Ta	0.003	0.004	0.003	0.001	0.003	<dl	0.007	0.001
La	0.171	0.373	0.203	0.022	0.111	0.067	0.276	0.683
Ce	0.517	1.072	0.648	0.070	0.369	0.214	0.213	1.109
Pb	0.158	0.290	0.127	0.045	0.051	0.126	0.098	0.191
Pr	0.107	0.231	0.135	0.020	0.106	0.045	0.038	0.106
Sr	59.047	18.824	23.838	20.851	29.300	41.800	8.130	6.850
Nd	0.703	1.428	0.810	0.156	0.641	0.284	0.239	0.162
Zr	3.405	5.411	3.312	0.495	4.260	1.109	1.519	0.300
Hf	0.134	0.234	0.133	0.025	0.197	0.051	0.073	0.007
Sm	0.319	0.585	0.370	0.109	0.300	0.161	0.131	0.006
Eu	0.153	0.181	0.155	0.078	0.125	0.096	0.058	0.002
Gd	0.595	0.817	0.691	0.216	0.416	0.281	0.271	0.011
Tb	0.114	0.132	0.130	0.044	0.071	0.063	0.053	0.001
Dy	0.852	0.788	0.942	0.306	0.454	0.439	0.387	0.018
Y	5.391	4.565	6.172	1.828	2.870	2.750	2.780	0.164
Ho	0.187	0.162	0.220	0.072	0.101	0.094	0.093	0.006
Yb	0.537	0.408	0.605	0.180	0.241	0.268	0.304	0.046
Er	0.587	0.452	0.638	0.196	0.278	0.299	0.299	0.023
Lu	0.084	0.062	0.093	0.026	0.037	0.041	0.047	0.010
La/Yb	0.319	0.914	0.335	0.120	0.399	0.250	0.910	14.960
La/Nb	6.622	16.349	7.094	1.816	2.015	7.440	4.890	61.210

<dl: below detection limit.  
n.a.: no available.

Table 5. Isotopic compositions of investigated rocks

Rock	Sample No.	$^{147}\text{Sm}/^{144}\text{Nd}$	$^{143}\text{Nd}/^{144}\text{Nd}$	$(^{143}\text{Nd}/^{144}\text{Nd})_i$	$\epsilon(\text{Nd})_i$	Rb	$^{87}\text{Sr}/^{86}\text{Sr}$	$(^{87}\text{Sr}/^{86}\text{Sr})_i$	$\epsilon(\text{Sr})_i$
Basalt	02SQ3	0.095	$0.512755 \pm 6$	0.5126931	3.6	36.40	$0.703997 \pm 8$	0.70376	-8.8
Basalt	03G12	0.204	$0.512979 \pm 9$	0.5128453	6.6	1.30	$0.703814 \pm 9$	0.70373	-9.2
Dolerite	02GU10	0.15	$0.513017 \pm 6$	0.5129188	8.0	0.68	$0.703782 \pm 10$	0.703748	-9.0
Dolerite	02GU11A	0.128	$0.512988 \pm 6$	0.512904	7.7	0.28	$0.703449 \pm 8$	0.703447	-13.3
Dolerite	02GU16	0.149	$0.513031 \pm 6$	0.5122963	8.8	5.37	$0.703946 \pm 8$	0.70374	-9.1
Gabbro	02GU12A	0.949	$0.512948 \pm 8$	0.5122767	5.0	0.76	$0.703466 \pm 9$	0.703434	-13.5
Gabbro	02GU8A	0.073	$0.512933 \pm 9$	0.5128852	7.3	26.80	$0.705889 \pm 8$	0.704885	7.1
Gabbro	03G21	0.009	$0.512968 \pm 7$	0.5129623	8.8	14.60	$0.705961 \pm 10$	0.705087	10.0
Granul	02GU12	0.171	$0.513009 \pm 6$	0.5128973	7.6	0.18	$0.703866 \pm 6$	0.703855	-7.5
Amph	02GU6	0.146	$0.513010 \pm 6$	0.5129163	7.9	0.55	$0.703550 \pm 8$	0.703534	-12.0
Amph	03G23	0.212	$0.512952 \pm 3$	0.5128132	5.9	4.31	$0.704125 \pm 8$	0.703898	-6.9
Amph	04SQ3	0.243	$0.513005 \pm 10$	0.5125093	6.6	0.86	$0.703427 \pm 7$	0.703414	-13.7
Amph	03SQ9	0.573	$0.512987 \pm 7$	0.5126119	2.0	13.99	$0.703894 \pm 8$	0.703926	-6.5
B-amph	04GU8	0.257	$0.513011 \pm 7$	0.5128431	6.5	2.20	$0.703761 \pm 8$	0.703607	-11.0
B-amph	04GU12	0.237	$0.512894 \pm 9$	0.5128785	4.9	4.14	$0.704479 \pm 8$	0.704122	-3.7
B-amph	03G22B	0.232	$0.512752 \pm 10$	0.5126001	1.8	2.09	$0.703716 \pm 7$	0.703579	-11.4
M-schist	04SJ1	0.137	$0.512673 \pm 6$	0.512678	1.06	41.30	$0.706278 \pm 7$	0.705866	20.2
M-schist	04SJ6	0.118	$0.512847 \pm 1$	0.5128397	4.5	80.30	$0.708444 \pm 16$	0.706530	29.9
Melagabb	03SJ4	0.276	$0.513027 \pm 10$	0.5128522	6.7	0.34	n.a.	n.a.	n.a.
Melagabb	03G18	0.248	$0.513032 \pm 9$	0.51287	7.0	0.36	$0.703535 \pm 9$	0.703456	-13.2
Melagabb	03SJ3	n.a.	n.a.	n.a.	n.a.	0.23	n.a.	n.a.	n.a.
Pyrox	03SQ22	n.a.	n.a.	n.a.	n.a.	0.30	n.a.	n.a.	n.a.
Pyrox	04SQ11	0.232	$0.513028 \pm 15$	0.5126001	6.5	0.50	$0.703553 \pm 7$	0.703482	-12.8
Lherz	03SJ2	n.a.	n.a.	n.a.	n.a.	n.a.	n.a.	n.a.	n.a.
Lherz	03SQ18	n.a.	n.a.	n.a.	n.a.	n.a.	n.a.	n.a.	n.a.
Harzb	98SQ3	n.a.	n.a.	n.a.	n.a.	n.a.	n.a.	n.a.	n.a.

using the procedures described in Cotten *et al.* (1995). Trace elements including the rare earth elements (REE) were analyzed by ICP-MS analysis at the Université Joseph Fourier in Grenoble, after acid dissolution of 100 mg sample, using the procedures of Barrat *et al.* (1996). Standards used for the analyses were BR-24, BR-22 and Bir-1. Analytical errors are 1–3% for major elements and lesser than 3% for trace elements. All the samples were pulverized using an agate mill.

Sr (static acquisition) and Nd (dynamic acquisition) isotopic ratios were measured on 26 samples at the Laboratoire de Géochimie Isotopique de l'Université Paul Sabatier de Toulouse on a Finnigan MAT 261 multicollector massspectrometer using the analytical procedures of Lapierre *et al.* (1997). Results on the Rennes standards (Chauvel and Blichert-Toft, 2001) yielded  $^{143}\text{Nd}/^{144}\text{Nd}$  values of  $0.51196 \pm 0.00002$  on 10 standards. Results on NBS 987 Sr standards yielded  $^{87}\text{Sr}/^{86}\text{Sr}$

$= 0.710254 \pm 0.000004$  on 15 standard determinations.  $^{87}\text{Sr}/^{86}\text{Sr}$  and  $^{143}\text{Nd}/^{144}\text{Nd}$  were normalized for mass fractions relative to  $^{87}\text{Sr}/^{86}\text{Sr} = 0.1194$  and  $^{143}\text{Nd}/^{144}\text{Nd} = 0.7219$  respectively.  $\epsilon\text{Nd}_i$  was calculated with actual  $(^{143}\text{Nd}/^{144}\text{Nd})_{\text{CHUR}} = 0.512638$  and  $(^{147}\text{Sm}/^{144}\text{Nd})_{\text{CHUR}} = 0.1967$ .  $\epsilon\text{Sr}_i$  was calculated with actual  $(^{87}\text{Sr}/^{86}\text{Sr})_{\text{CHUR}} = 0.70450$  and  $(^{87}\text{Rb}/^{86}\text{Sr})_{\text{CHUR}} = 0.084$  (McCulloch and Wasserburg, 1978). Before acid digestion and Nd and Sr chemical separations, leaching with 2.5 N HCl was carried out at 100°C in two steps, each one lasting 20 min.

For lead separation, eighteen powdered samples of approximately 300 ng of lead were prepared. A leaching step with 6N HCl during 20 min at 65°C was done before acid digestion. Samples were then dissolved during 48–72 h on a hotplate with a mixing of tri-distilled Hf:HNO<sub>3</sub> concentrated acids. After evaporation of dryness, 1 ml of HNO<sub>3</sub> was added to the residue and kept at 70° for 2–3 h before complete evaporation. Lead was chemically sepa-

Table 5. (continued)

Rock	Sample No.	$^{206}\text{Pb}/^{204}\text{Pb}$	$2\sigma$	$(^{206}\text{Pb}/^{204}\text{Pb})_i$	$^{207}\text{Pb}/^{204}\text{Pb}$	$2\sigma$	$(^{207}\text{Pb}/^{204}\text{Pb})_i$	$^{208}\text{Pb}/^{204}\text{Pb}$	$2\sigma$	$(^{208}\text{Pb}/^{204}\text{Pb})_i$
Basalt	02SQ3	n.a.	n.a.	n.a.	n.a.	n.a.	n.a.	n.a.	n.a.	n.a.
Basalt	03G12	19.151	0.01	18.945	15.646	0.01	15.636	38.973	0.01	38.745
Dolerite	02GU10	18.95	0.01	18.87	15.56	0.01	15.55	38.59	0.01	38.5
Dolerite	02GU11A	n.a.	n.a.	n.a.	n.a.	n.a.	n.a.	n.a.	n.a.	n.a.
Dolerite	02GU16	19.3	0.01	18.93	15.68	0.01	15.67	39.16	0.01	38.78
Gabbro	02GU12A	18.97	0.01	18.97	15.663	0.01	15.663	38.797	0.02	38.788
Gabbro	02GU8A	19.158	0.01	19.064	15.692	0.02	15.688	38.811	0.02	38.755
Gabbro	03G21	18.826	0.01	18.82	15.71	0.02	15.71	39.19	0.02	39.17
Granul	02GU12	19.075	0.01	19.074	15.687	0.01	15.686	38.94	0.02	38.936
Amph	02GU6	18.94	0.01	18.77	15.67	0.01	15.65	38.79	0.01	38.61
Amph	03G23	19.25	0.02	19.05	15.71	0.02	15.69	39.19	0.02	38.98
Amph	04SQ3	18.7782	0	18.723	15.5737	0	15.571	38.832	0	38.776
Amph	03SQ9	18.7604	0.01	18.7234	15.605	0.01	15.6032	38.419	0.01	38.402
B-amph	04GU8	n.a.	n.a.	n.a.	n.a.	n.a.	n.a.	n.a.	n.a.	n.a.
B-amph	04GU12	19.0590	0	18.9766	15.5593	0	15.5553	38.544	0	38.517
B-amph	03G22B	18.9457	0.02	18.8373	15.6216	0.02	15.6163	38.5802	0.02	38.5105
M-schist	04SJ1	18.6079	0	18.5674	15.602	0.01	15.6	38.4853	0.01	38.4383
M-schist	04SJ6	18.6221	0	18.1328	15.5951	0	15.57186	38.46	0	37.9322
Melagabb	03SJ4	18.659	0.01	18.627	15.564	0.01	15.562	38.26	0.01	38.1
Melagabb	03G18	18.82	0.02	18.8	15.67	0.02	15.66	38.55	0.02	38.22
Melagabb	03SJ3	n.a.	n.a.	n.a.	n.a.	n.a.	n.a.	n.a.	n.a.	38.52
Pyrox	03SQ22	18.430	0.01	18.43	15.502	0.01	15.502	38.11	0.02	n.a.
Pyrox	04SQ11	n.a.	n.a.	n.a.	n.a.	n.a.	n.a.	n.a.	n.a.	n.a.
Lherz	03SJ2	n.a.	n.a.	n.a.	n.a.	n.a.	n.a.	n.a.	n.a.	n.a.
Lherz	03SQ18	n.a.	n.a.	n.a.	n.a.	n.a.	n.a.	n.a.	n.a.	n.a.
Harzb	98SQ3	n.a.	n.a.	n.a.	n.a.	n.a.	n.a.	n.a.	n.a.	n.a.

n.a.: not available.

rated using anion exchange resin (AG1X8, 200–400 mesh) and samples were loaded and washed in 0.5N HBr. Lead was then eluted in 6 N HCl. Pb blanks were less than 40 pg and are negligible for the present analyses.

Lead isotope analyses were carried out using a VG model Plasma magnetic sector-inductively coupled plasma-mass spectrometer (MC-ICP-MS) at the Ecole Normale Supérieure de Lyon. Lead isotope compositions were measured using the Tl normalization method described by White *et al.* (2000). For Pb isotope analyses, samples were bracketed between NIST 981 standards, and calculated with respect to the value reported for this standard by Todt *et al.* (1996). This technique yields internal precision of *ca.* 50 ppm ( $2\sigma$ ) and an external reproductibility of *ca.* 250 ppm  $2\sigma$  or  $^{206}\text{Pb}/^{204}\text{Pb}$  ratios determined on 20 NIST standards. All the isotopic data have been corrected for *in situ* decay using a mean age of 100 Ma, based on the Cretaceous ages of the accreted oceanic terranes. Only the mica-schists have been corrected using a mean age of 50 Ma, on the basis of the Andes exhumation event (e.g., Spikings *et al.*, 2001).

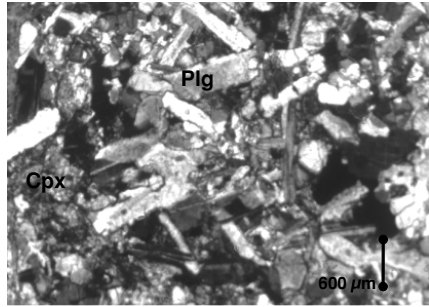
## RESULTS

### *Petrology and chemistry of the igneous and metamorphic rocks*

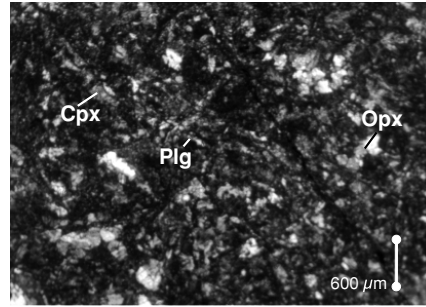
Basalts, dolerites and gabbros are the main facies of the igneous rock-type. Among the metamorphic rocks are amphibolites, mafic granulites, amphibolitized gneiss and garnet-bearing micaschists. The ultramafic rocks consist of lherzolites, harzburgites and clinopyroxenites. Petrological observations are presented in Table 1, and geochemical data are summarized in Tables 2 to 5.

#### *Igneous rocks*

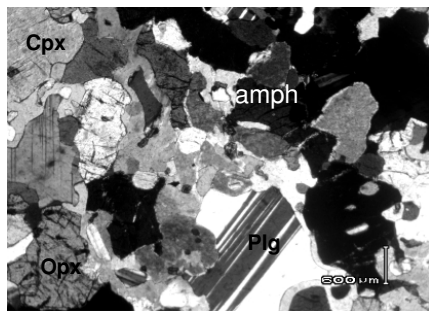
**Basalts and dolerites** In the basalts, the glass is commonly recrystallized in chlorite. Sample 03G12 groundmass includes quartz–chlorite-filled vesicles and calcite–epidote-filled cracks. Sample 02SQ3 exhibits preserved orthopyroxene, zoned plagioclase and early-crystallized oxides included in the pyroxenes (Plate 1b). The dolerites are characterized by ophitic texture (Table 1, Plate 1a). 02GU16 differs from the other dolerites by centimeter-sized clinopyroxene and serpentine + chlorite



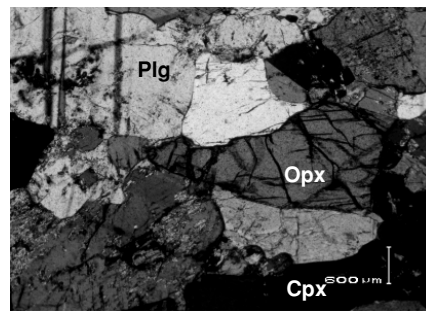
1a. Dolerite: 02GU11A. Clinopyroxene and plagioclase. Ophitic texture. (Crossed polars)



1b. Basalt: 02SQ3. Orthopyroxene, clinopyroxene, plagioclase and oxide. (Crossed polars)



1c. Gabbro: 02GU12A. Clinopyroxene + orthopyroxene + amphibole + plagioclase. Mesocumulate texture. (Crossed polars)



1d. Gabbro: 03G21. Clinopyroxene + orthopyroxene + plagioclase. Mesocumulate texture. (Crossed polars)

*Plate 1. Thin sections of igneous rocks.*

pseudomorphs after olivine.

In dolerite 02GU16, the clinopyroxene composition is Mg-rich augite ( $Wo_{40-50}$ ,  $En_{55-42}$ ,  $Fs_{11-22}$ ). Plagioclase crystals contain between 50% and 75% An (labradorite-bytownite). Dolerites and basalts are relatively rich in Mg ( $6 < MgO\% < 10$ ) and  $K_2O$ -poor ( $< 0.3\%$ ). The dolerites show relatively high Ti content ( $\geq 1$ ) (Table 2).

The flat chondrite-normalized REE patterns (Sun and McDonough, 1989) [ $(La/Yb)_N = 0.9$ ] of the dolerites are similar to those of the amphibolites. The primitive mantle-normalized multi-element (Sun and McDonough, 1989) patterns of the dolerites are almost flat and differ from each other by positive or negative Pb, Sr and Ti anomalies. Sr and Ti anomalies suggest accumulation or removal of plagioclase and magnetite, respectively. Sample 02GU10 differs from the other dolerites by Zr and Hf negative anomalies. The La/Nb ratio of these dolerites is less than 1 (Fig. 3a).

The trace element chemistry of two basalts (03G12, 02SQ3) differs significantly from each other. REE and trace element plots of sample 03G12 are similar to those

of the dolerites (flat with no Nb and Ta negative anomalies). Thus, dolerites and 03G12 basalt display geochemical features of oceanic plateau basalts. In contrast, sample 02SQ3 is characterized by LREE-enriched chondrite-normalized pattern [ $(La/Yb)_N = 8.1$ ] La/Nb ratio  $> 1$  (2.65) (Table 2), and Nb and Ta negative anomalies. Moreover, sample 02SQ3 exhibits marked Pb and Sr positive anomalies, likely due to plagioclase accumulation. Therefore, we interpret 02SQ3 basalt as developed in an arc or active margin environment (Fig. 3b).

**Gabbros** The gabbros usually show mesocumulate textures, and a magmatic layering is observed in sample 03G21 (Table 1; Plates 1c and 1d). In samples 02GU12A and 03G21, the crystallization sequence is as follows: plagioclase–orthopyroxene–clinopyroxene–amphibole. In sample 03G21, Fe–Ti oxide (4% vol) is the last mineral to precipitate. Orthopyroxene and plagioclase are sometimes replaced by chlorite and sericite, respectively. Sample 02GU8A is an altered cumulate gabbro: the clinopyroxene is replaced by an association of pale green hornblende and colourless actinolite, and plagioclase is

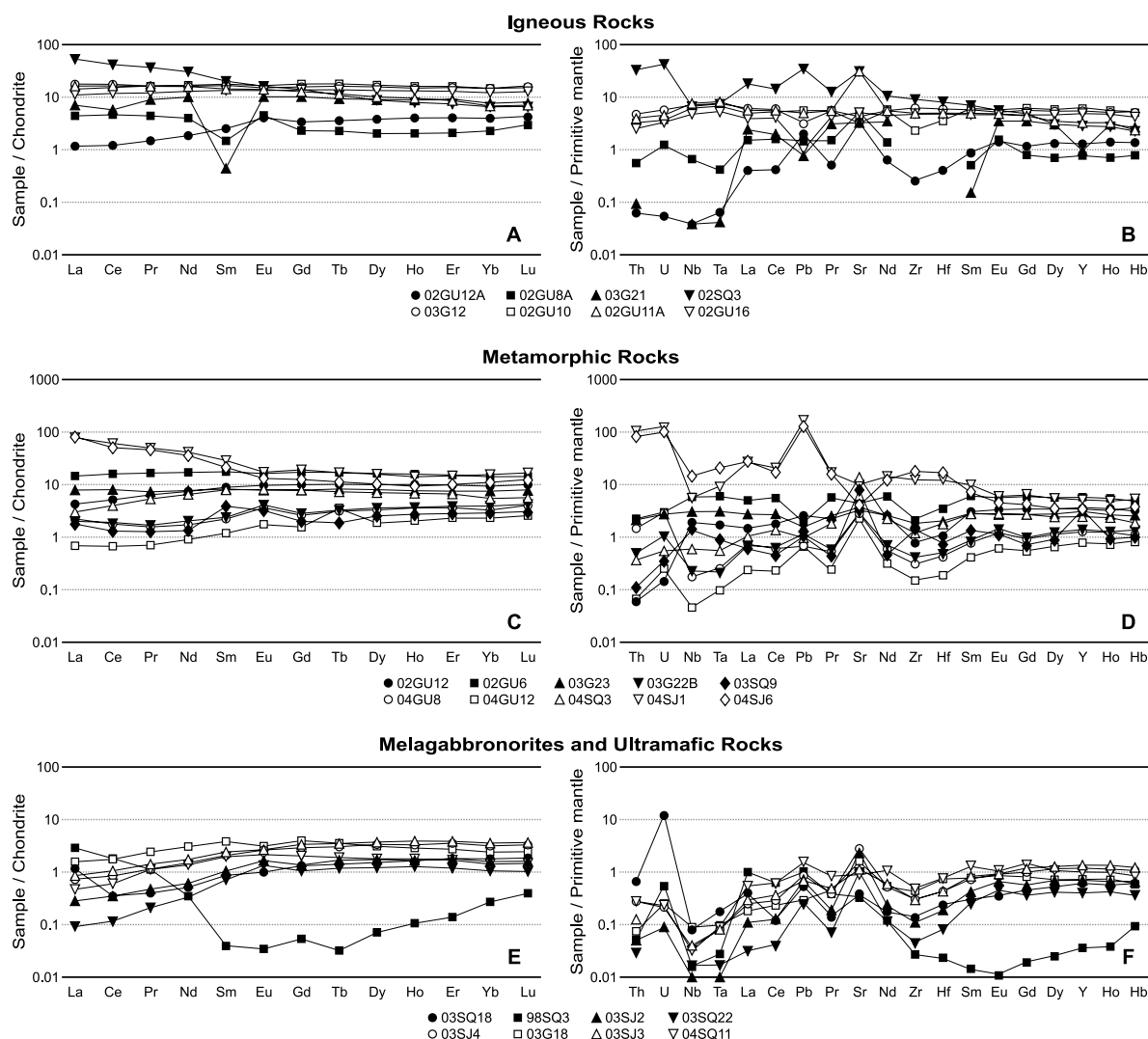


Fig. 3. Rare earth elements (REE) and incompatible trace elements normalized to chondrites and primitive mantle respectively (Sun and McDonough, 1989). 3a REE plot of igneous rocks. 3b Trace elements of igneous rocks. 3c REE of metamorphic rocks. 3d Trace elements of metamorphic rocks. 3e REE of melagabbro and ultramafic rocks. 3f Trace elements of melagabbro and ultramafic rocks.

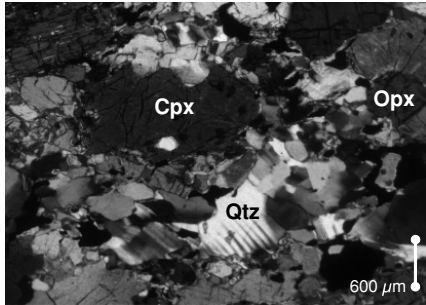
seldom preserved and is altered to sericite.

In the orthopyroxene–clinopyroxene gabbros, plagioclase composition ranges from  $An_{90}$  to  $An_{82}$  (anorthite–bytownite). In sample 03G21, clinopyroxene shows a diopside composition ( $Wo_{46}$ ,  $En_{41}$ ,  $Fs_{12}$ , Morimoto *et al.*, 1988) and the En content of the orthopyroxene is 67%. In sample 03G21,  $Fe_2O_3$  content reflects augite and diopside pyroxenes. In both samples, late magmatic amphibole has a magnesio–hornblende composition, and is locally replaced by actinolite (02GU12A). Fe–Ti oxides are either ilmenite (02GU12A,  $TiO_2 = 50.4\%$ ,  $FeO = 30\%$ ,  $Fe_2O_3 = 4.7\%$ ) or magnetite (03G21,  $TiO_2 = 2.6\%$ ,  $FeO = 33\%$ ,  $Fe_2O_3 = 60\%$ ).

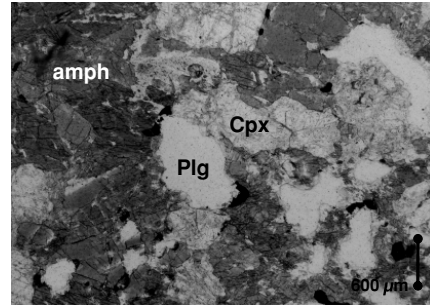
Gabbros have rather homogeneous major element

compositions. These cumulate rocks are MgO-,  $Al_2O_3$ - and CaO-rich and Ti-poor. The higher content in  $Fe_2O_3$  of sample 03G21 is due to the presence of late crystallized oxides. Sample 02GU8A differs from the two others by higher MgO and lower CaO contents, respectively (Table 2).

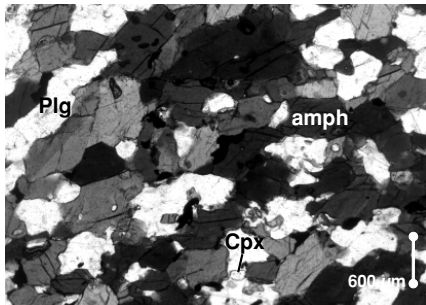
On the basis of the trace element contents and chondrite-normalized REE patterns (Sun and McDonough, 1989), sample 02GU8A is very different from the two opx–cpx gabbros (Fig. 3a). The 02GU8A REE pattern is slightly depleted in HREE [ $(La/Yb)_N = 1.9$ ] while those of samples 02GU12A and 03G21 are LREE-depleted [ $0.2 < (La/Yb)_N < 0.6$ ]. However, sample 03G21 differs from sample 02GU12A in having higher



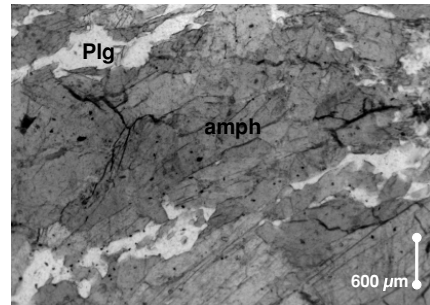
2a. Granulite: 02GU12. Orthopyroxene + clinopyroxene + quartz. (Crossed polars)



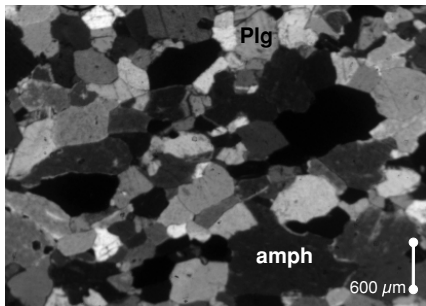
2b. Amphibolite: 03SQ9. Clinopyroxene-free. Large grain size. (Plane polarized-light)



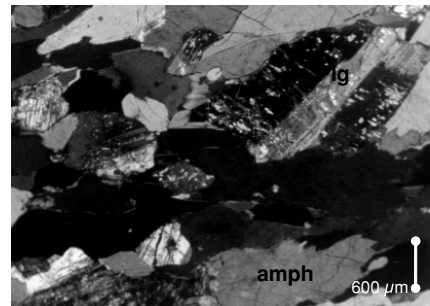
2c. Amphibolite: 02GU6. Plagioclase poor. Amphibole + clinopyroxene + plagioclase. Nematoblastic texture. (Plane polarized-light)



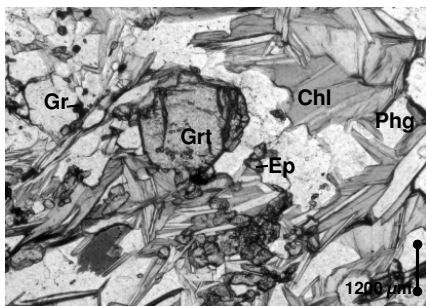
2d. Amphibolite: 03GU23. Plagioclase poor. (Plane polarized-light)



2e. Banded amphibolite: 03GU22B. Plagioclase + amphibole. Granoblastic texture. (Crossed polars)



2f. Banded amphibolite: 03G23. Plagioclase poor. (Crossed polars)



2g. Micaschist: 04SJ1. Garnet + chlorite + epidote and graphite. (Plane polarized-light)

*Plate 2. Thin sections of metamorphic rocks.*

HREE contents. All the gabbros show marked Eu [ $\text{Eu}/\text{Eu}^* = 1.7$ ] and Sr positive anomalies due to plagioclase accumulation. Primitive mantle-normalized (Sun and McDonough, 1989) diagrams of the two orthopyroxene-clinopyroxenes gabbros are characterized by depletion in Th, U, Nb and Ta which is absent in sample 02GU8A.

#### *Metamorphic rocks*

*Mafic granulite* In this study mafic granulite (02GU12) is represented by a two-pyroxene-plagioclase-quartz metabasite that equilibrated under granulite facies conditions ( $T = 800\text{--}850^\circ\text{C}$ ,  $P < 6\text{--}9$  kbars; Beaudon *et al.*, 2005). This metamorphic mafic rock consists of diopside ( $\text{Wo}_{43.58\text{--}45.67}$ ,  $\text{En}_{40.34\text{--}40.96}$ ,  $\text{Fs}_{13.99\text{--}15.46}$ ) systematically associated with enstatite ( $\text{Wo}_{1.34\text{--}1.51}$ ,  $\text{En}_{60.85\text{--}61.95}$ ,  $\text{Fs}_{36.71\text{--}37.64}$ ) and quartz. Small-sized magnesio-hornblende can be recognized at the rim of pyroxenes. Elongated enstatite grains outline the weak foliation (Plate 2a).

The chondrite-normalized REE pattern of this granulite is LREE-depleted [ $(\text{La}/\text{Yb})_{\text{N}} = 0.45$ ] and similar to those of MORB and to some Piñon dolerites, interpreted as accreted remnants of the Cretaceous Colombian-Caribbean oceanic plateau (CCOP, Reynaud *et al.*, 1999; Kerr *et al.*, 2002, Kerr, 2003; Mamberti *et al.*, 2003). The REE pattern of the granulite displays a positive Eu anomaly [ $(\text{Eu}/\text{Eu}^*) = 2.3$ ] due to plagioclase accumulation (Fig. 3c). The primitive mantle normalized multi-element plot (Sun and McDonough, 1989) of this granulite is characterized by depletion in Th, U, Zr and Hf and a small enrichment in Nb with respect to LREE. The La/Nb ratio is very low (0.77; see Fig. 3d).

*Amphibolites* Thermobarometric study of the amphibolites indicated crystallisation conditions of 800–850°C and 6–9 kb (20–25 km deep, Beaudon *et al.*, 2005). From one of these amphibolites, Vallejo *et al.* (2006) reported a  $84.69 \pm 2.23$  Ma age ( $^{40}\text{Ar}/^{39}\text{Ar}$  age on hornblend), interpreted as due to the plume-related thermal event associated with the oceanic plateau emplacement.

All studied amphibolites fine-grained, and present variable abundance of amphibole with respect to plagioclase. They are made of magnesio-hornblende, clinopyroxene, plagioclase, oxides and sphene (Table 1; Plates 2b and 2c). Texture varies from heteroblastic nematoblastic to foliated (Plates 2c and 2d).

Amphibole falls in the magnesio-hornblende field (Leake *et al.*, 1997) but is more Fe-rich when associated with diopside. Plagioclase composition varies from bytownite ( $\text{An}_{80\text{--}85}$ , 03G23, 04GU12) to labradorite ( $\text{An}_{55}$ , 02GU6). In sample 03G23, clinopyroxene shows a diopside homogeneous composition ( $\text{Wo}_{47\text{--}49}$ ,  $\text{En}_{34\text{--}35}$ ,  $\text{Fs}_{18\text{--}20}$ ; Morimoto *et al.*, 1988). Based on their MgO content, the amphibolites have mafic rock compositions ( $10 > \text{MgO}\% > 6$ ). The  $\text{TiO}_2$  and  $\text{Fe}_2\text{O}_3$  abundances of the

most mafic amphibolites (02GU6, 03G23) suggest a tholeiitic affinity. These amphibolites are K-poor (Table 3).

The chondrite-normalized REE patterns of the amphibolites are flat [ $(\text{La}/\text{Yb})_{\text{N}} \sim 1$ ] (Fig. 3c), or depleted in LREE [04SQ3, 03SQ9,  $0.9 < (\text{La}/\text{Yb})_{\text{N}} < 0.5$ ]. Sample 04SQ3 shares similar LREE-depleted patterns with the granulite. The amphibolites show small negative and/or positive Eu anomalies ( $1.5 < \text{Eu}/\text{Eu}^* < 0.9$ ). The primitive mantle-normalized multi-element plots of the amphibolites are of two types (Fig. 3d). The first one is characterized by flat patterns with a slight depletion in Th (02GU6, 03G23). The second type differs from the previous one by marked positive Sr anomaly, and depletion in Th and U (03SQ9, 04SQ3). Sample 03SQ9 differs from the other amphibolites by enrichment in Hf and Sm. The marked Sr positive anomaly reflects plagioclase accumulation. None of these multi-element plots exhibits negative Nb and Ta anomalies. The La/Nb ratio of these amphibolites is  $< 1$  (Table 3).

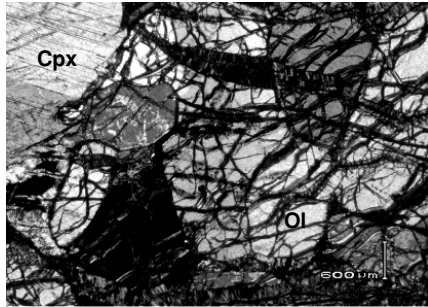
*Banded amphibolites* The banded amphibolites show coarse grain size, granoblastic textures and a marked foliation (Table 1; Plate 2e). Locally, large minerals formed of a chlorite-serpentine association probably represent orthopyroxene pseudomorphs. Sample 04GU12 exhibits a porphyroblastic granoblastic texture (Plate 2f); the porphyroblasts are formed of plagioclase grains (up to 1.2 mm in size) often replaced by sericite, while hornblende layers are finer grained (up to 0.5 mm) and locally contain actinolite needle-shaped crystals. Late epidote-filled cracks crosscut the metamorphic foliation.

Only minerals of sample 04GU12 have been analyzed. Pleochroic green amphibole has magnesio-hornblende composition (Leake *et al.*, 1997). Plagioclase is Ca-rich and its An content varies from 75 to 86%. Banded amphibolites are Ca- and Mg-rich and Ti-poor (Table 3).

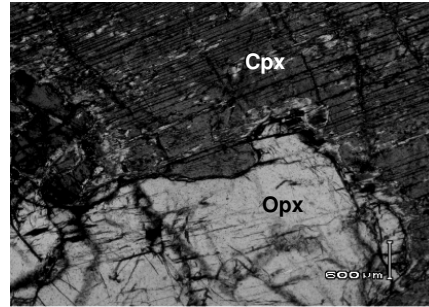
Their chondrite-normalized REE patterns are LREE-depleted [ $0.75 < (\text{La}/\text{Yb})_{\text{N}} < 0.51$ ] with the exception of marked Eu ( $1.8 < \text{Eu}/\text{Eu}^* < 1.65$ ) positive anomalies related to plagioclase accumulation (Fig. 3c). Their primitive-mantle normalized multi-element plots (Fig. 3d; Sun and McDonough, 1989) are characterized by positive U, Pb, Sr and Eu anomalies, and by negative Nb, Ta, Zr and Hf anomalies. Positive Pb, Eu, Sr anomalies can be attributed to plagioclase accumulation while the HFSE negative anomalies are probably linked to the presence of clinopyroxene, a mineral known to have low Kd values for these elements.

*Micaschists* Thermobarometric study of the micaschists supports peak metamorphic conditions at 300–380°C and 5.5 to  $< 8$  kb. This indicates peak metamorphism under HP-BT conditions, and suggests that it took place in a subduction zone (Amórtégui, 2008).

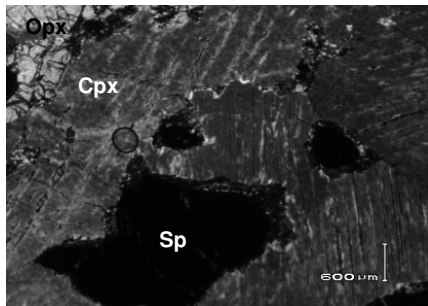
The quartz-micaschists (Table 1) are fine- (1–0.1 mm)



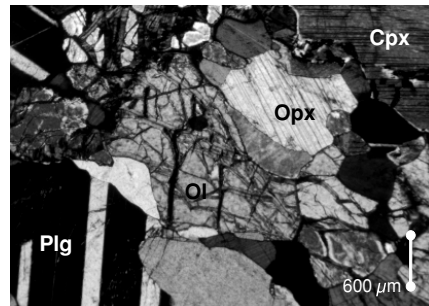
3a. Melagabbronorite: 03SJ3. Olivine + clinopyroxene ± plagioclase. Cumulate texture. (Crossed polars)



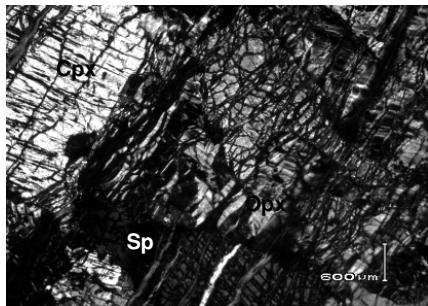
3b. Melagabbronorite: 03SJ4. Orthopyroxene + clinopyroxene ± plagioclase. adcumulate texture. (Crossed polars)



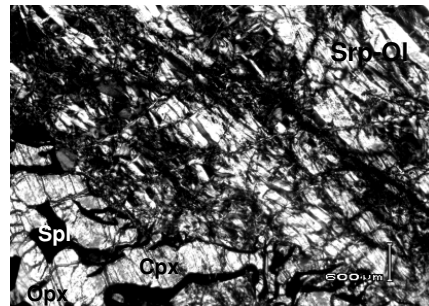
3c. Pyroxenite: 03SQ22. Orthopyroxene + clinopyroxene + green spinel. (Crossed polars)



3d. Lherzolite: 03SJ2. Orthopyroxene + clinopyroxene + plagioclase + olivine. (Crossed polars)



3e. Lherzolite: 03SQ18. Orthopyroxene + clinopyroxene + green spinel. Blastomylonitic texture. (Crossed polars)



3f. Harzburgite: 98SQ3. Serpentinized olivine + orthopyroxene + clinopyroxene + red spinel. (Crossed polars)

Plate 3. Thin sections of melagabbronorites and ultramafic rocks.

to medium-grained (1–4 mm) and intensely micro-folded. Sample 04SJ1 includes epidote (15% vol; Plate 2g), and 04SJ6 is richer in graphite (50% vol). Samples 04SJ6 and 04SJ1 differ in that they bear chloritoid and garnet, respectively.

White mica of phengite composition occurs in both samples (04SJ1:  $Al_{3.2-3.5}, Si_6, Mg_{0.8-2}$ , and 04SJ6:  $Al_{3.4-3.8}, Si_6, Mg_{0.1-0.5}$ ). Chlorite composition is that of a corundophyllite ( $Si_{4.2}, Fe^{2+} + Fe^{3+}_{2.8}$ ) trending towards talc–chlorite. Chloritoid composition is  $Fe^{2+}_{3.2}, Si_3, Al_{3.5}$ .

Micaschists have very homogeneous major element compositions, close to that of the continental crust ( $SiO_2$ : 60–70%;  $Al_2O_3$ : 16%; Table 3; Taylor and McLennan, 1985).

The chondrite-normalized REE patterns of these micaschists are also similar to that of the Bulk Continental Crust (BCC; Taylor and McLennan, 1985) (Fig. 3c) with a characteristic LREE-enrichment [ $5 < La/Yb_N < 7.3$ ] and a marked negative Eu anomaly [ $Eu/Eu^* = 0.8$ ]. The abundance of all trace elements in these micaschists (Table 3) is probably due to the presence of organic mat-

ter. These show positive anomalies in Th, U and Pb (Fig. 3d).

#### *Melagabbronorites and ultramafic rocks*

*Melagabbronorites and pyroxenites* Among the igneous ultramafic rocks, pyroxene-rich rocks are the most abundant and diverse (Table 1). They show adcumulate and heteradcumulate textures and can be called melagabbronorites. Sample 03SJ3 (Plate 3a) consists of cumulus olivine included in 1 to 2.5 mm long clinopyroxene grains (locally deformed in kink bands), of plagioclase as intercumulus phase, and of scarce euhedral oxides may be present. Clinopyroxene shows orthopyroxene exsolutions or includes tiny orthopyroxene grains. The mineral crystallization sequence is as follows: olivine, orthopyroxenes, clinopyroxene, plagioclase, and oxides. 03SJ4 (Plate 3b) is olivine-free. Clinopyroxene rims in contact with plagioclase are altered into actinolite. Locally, fracture veins filled with recrystallized anhedral grains of altered (actinolite) clinopyroxene and plagioclase cross cut the rock. 03G18 is a clinopyroxene-orthopyroxene adcumulate with few altered plagioclase. Clinopyroxene is deeply altered into actinolite while orthopyroxene is entirely replaced by talc.

The foliated pyroxenites (03SQ22, 04SQ11) consist of clinopyroxene, orthopyroxene, green spinel (pleonaste) and locally serpentinized olivine (Table 1; Plate 3c). The foliation is marked by the elongated and deformed orthopyroxene. Clinopyroxene occurs as large (up to 8 mm-sized) crystals. Anhedral spinels are included into, or are located between, the pyroxenes.

With the exception of sample 03SJ3, all clinopyroxene exhibit very homogeneous diopside compositions ( $Wo_{48}$ ,  $En_{45-48}$ ,  $Fs_{2-6}$ ). In sample 03SJ3, clinopyroxene shows an evolution from diopside ( $Wo_{48}$ ,  $En_{44}$ ,  $Fs_7$ ) to augite ( $Wo_2$ ,  $En_{80}$ ,  $Fs_{17}$ , Fig. 4) marked by enrichment in Mg relative to Ca.

Sample 03SJ4 is the most  $Al_2O_3$ -rich because of the abundance of plagioclase, while sample 03G18 is the most  $SiO_2$ -rich because orthopyroxene predominates over clinopyroxene (Table 4). The higher MgO content of sample 03SJ3 compared to the other pyroxenites is due to the presence of olivine.

The chondrite-normalized REE patterns of the pyroxenites are similar to those of pyroxenites, i.e., depleted in LREE [ $(La/Yb)_N$  between 0.1 and 0.3]. The REE patterns show positive (03SQ22,  $Eu/Eu^* = 1.6$ ), or negative (03G18,  $Eu/Eu^* = 0.8$ ) Eu anomalies, suggesting plagioclase accumulation or removal. Foliated pyroxenites, such as in samples 03SQ22 and 04SQ11, have very low REE contents (<1 times the chondritic value, especially for the LREE), and thus differ from the cumulate pyroxenites (Fig. 3e).

The primitive mantle-normalized multi-element diagrams of the pyroxenites are characterized by positive U,

Pb and Sr anomalies, negative Zr and Hf anomalies, and flat HREE compatible element patterns (Fig. 3f).

Sample 03G18 differs from the other pyroxenites by the absence of a positive Sr anomaly. The foliated pyroxenites differ from the cumulate rocks by having lower trace element contents (less than 0.1 the primitive mantle abundance, especially for the incompatible elements such as Nb, Ta, La), and the most marked Zr and Hf negative anomalies.

*Lherzolites* In the plagioclase lherzolite (03SJ2, Table 1, Plate 3d), foliation is marked by elongated and deformed pyroxene crystals. Olivine is partly replaced by serpentine and iddingsite. Plagioclase is sometimes included in the orthopyroxene but occurs also as aggregates formed of anhedral and undeformed crystals. Orthopyroxene is most often altered in talc, while clinopyroxene is preserved and exhibits orthopyroxene exsolutions along cleavages. Plagioclase-free lherzolite (03SQ18, Plate 3e) shows blastomylonitic texture marked by dominant serpentinized olivine, orthopyroxene crystals, and Al-rich green spinel.

In both rocks, clinopyroxene exhibits diopside composition ( $Wo_{46}$ ,  $En_{47}$ ,  $Fs_{4-7}$ ). Olivine ( $Fo_{90}$ ) and orthopyroxene ( $En_{89}$ ,  $Fs_9$ ,  $Wo_{1,2}$ ) are more Mg-rich in sample 03SQ18 compared to those of the plagioclase lherzolite (Olivine =  $Fo_{83}$ ; orthopyroxene =  $En_{82}$ ,  $Fs_{15}$ ,  $Wo_2$ ). Moreover, orthopyroxene and clinopyroxene in sample 03SQ18 display FeO and  $TiO_2$  enrichment from core to rim. Al-rich spinel exhibits a pleonaste composition ( $Cr/Cr + Al = 0.15$ ,  $Fe^{3+}/Fe^{3+} + Al + Cr = 0.2$ ,  $Fe^{3+} = 0.3$ ,  $Cr^{3+} = 2$ ,  $Al^{3+} = 14$ ). Plagioclase in sample 03SJ2 is anorthite ( $An_{90}$ ). Lherzolites are Mg-rich (Table 4) ( $20 < MgO\% < 35$ ) and  $TiO_2$ - and  $Na_2O$ -poor. The rather high  $Al_2O_3$  content (11.5%) of sample 03SJ2 is due to the presence of plagioclase.

Both foliated lherzolites are characterized by LREE-depleted patterns [ $0.2 < (La/Yb)_N < 0.6$ ] (Fig. 3e). Their primitive mantle-normalized multi-element diagrams exhibit very low trace element contents (about 0.01 to 0.1 the primitive mantle values) and negative Nb and Ta anomalies (Fig. 3f; Sun and McDonough, 1989). Sample 03SJ2 shows a positive Sr anomaly due to the presence of bytownite.

*Harzburgite* In the harzburgite (98SQ3, Table 1), the intense foliation is outlined by deformed and elongated orthopyroxene crystals (Plate 3f). Picotite forms a symplectitic texture with clinopyroxene. The high LOI (15.3%) of the harzburgite is due to the abundant serpentine (Table 4).

The harzburgite differs from the lherzolites by a lower CaO content, and its REE contents are very low (between 0.1 and 1 times the chondritic values, especially for the medium and heavy REE). The U-shaped chondrite-normalised REE pattern of this harzburgite is very simi-

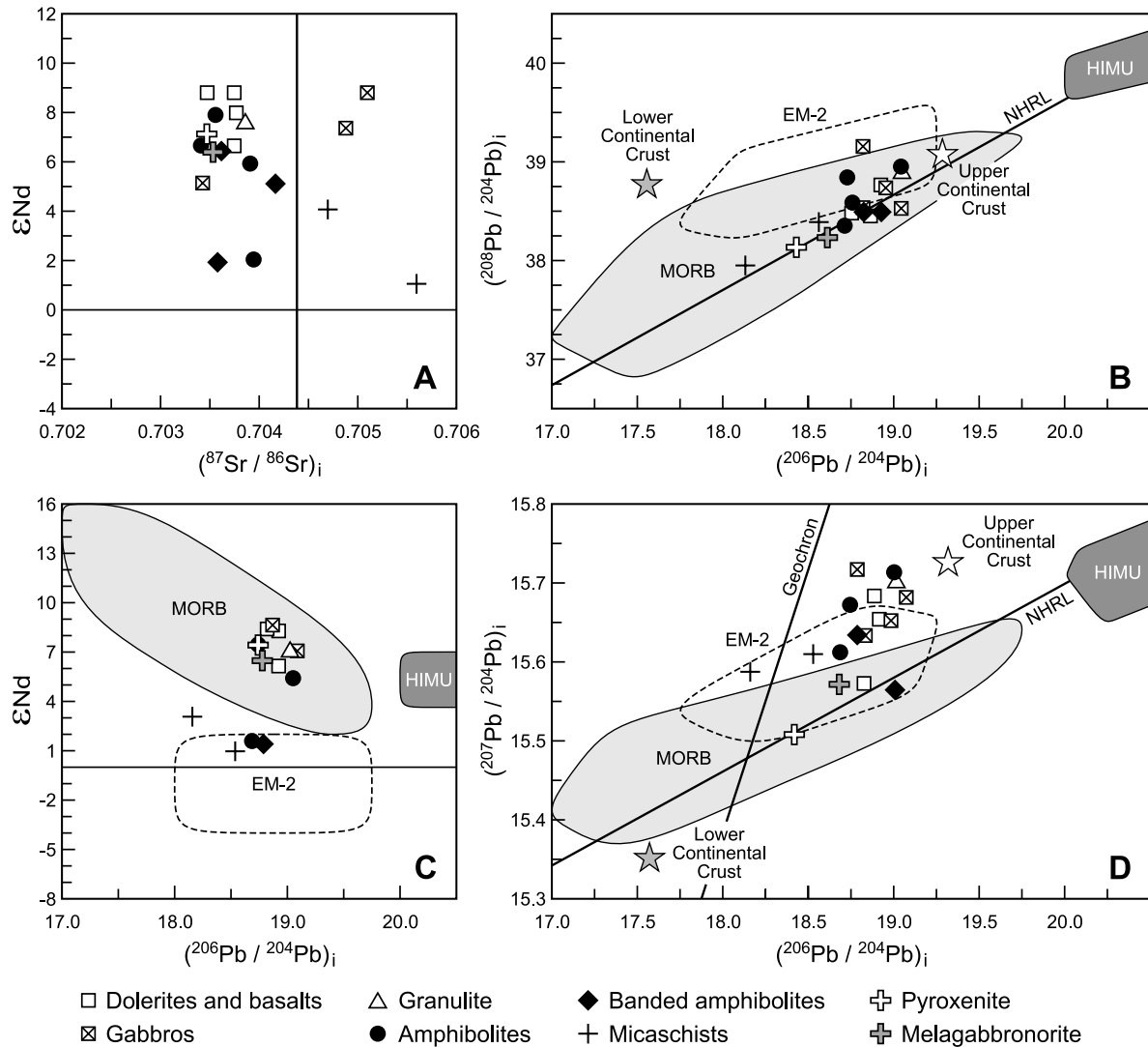


Fig. 4. Isotopic compositions of igneous, metamorphic and ultramafic rocks of Ecuador: A.  $\epsilon_{Nd}$  vs.  $(^{87}Sr/^{86}Sr)_i$ ; B.  $(^{208}Pb/^{204}Pb)_i$  vs.  $(^{206}Pb/^{204}Pb)_i$ ; C.  $(^{207}Pb/^{204}Pb)_i$  vs.  $(^{206}Pb/^{204}Pb)_i$ ; D.  $\epsilon_{Nd}$  vs.  $(^{206}Pb/^{204}Pb)_i$ . Present-day fields of MORB, OIB, EM-1, EM-2, HIMU, Upper and Lower continental crust after Hofmann (1997).

lar to those of depleted abyssal harzburgites (Sharma and Wasserburg, 1996; Fig. 3e). This REE pattern is also characterized by a negative Eu anomaly ( $Eu/Eu^* = 0.6$ ). The primitive mantle-normalized multi-element plot of the harzburgite is characterized by very low contents in incompatible elements (less than 0.1 of the primitive mantle abundance), positive U, Pb, Sr, and HREE anomalies, and negative Nb, Ta, Zr and Eu anomalies (Fig. 3f)

#### Isotopic compositions of igneous and metamorphic rocks

##### Igneous rocks

**Basalts and dolerites** The  $\epsilon_{Nd}$  values of the dolerites and basalt 03G12, with major and trace element characteristics of oceanic plateau affinities, range from +6.6 to

+8.8. The  $(^{87}Sr/^{86}Sr)_i$  ratios are more homogeneous and range between 0.703730 and 0.703748. The basalt with an arc affinity has a lower  $\epsilon_{Nd}$  value (+3.6) but its  $(^{87}Sr/^{86}Sr)_i$  falls in the range of those of the dolerites. In the  $\epsilon_{Nd}$  vs.  $(^{87}Sr/^{86}Sr)_i$  diagram (Fig. 4a), dolerites and basalts are shifted towards the higher  $(^{87}Sr/^{86}Sr)_i$  ratios. Dolerites and basalts have comparable initial Pb ratios (Table 5). In the lead/lead and/or  $\epsilon_{Nd}$  vs.  $(^{206}Pb/^{204}Pb)_i$  diagrams, dolerites and basalt plot between the MORB and EM II fields with the exception of one dolerite (02GU10) that plots in the MORB field (Figs. 4b, 4c and 4d).

**Gabbros** The gabbros have high positive  $\epsilon_{Nd}$  values (5.0, +7.3 and +8.8, respectively; Table 5). In the  $\epsilon_{Nd}$  vs.  $(^{87}Sr/^{86}Sr)_i$  diagram (Fig. 4a), samples 02G8A and 03G21

are shifted towards high  $(^{87}\text{Sr}/^{86}\text{Sr})_i$  ratios, while sample 02G12A has a relatively low  $(^{87}\text{Sr}/^{86}\text{Sr})_i$  value. In the  $(^{208}\text{Pb}/^{204}\text{Pb})_i$  and  $(^{207}\text{Pb}/^{204}\text{Pb})_i$  vs.  $(^{206}\text{Pb}/^{204}\text{Pb})_i$  diagrams (Figs. 4b and 4c), the three gabbros plot above the NHRL line and in the EMII field. In the  $\epsilon_{\text{Nd}}$  vs.  $(^{206}\text{Pb}/^{204}\text{Pb})_i$  correlation diagram (Fig. 4d), samples 02GU8A and 03G21 plot near and/or in the MORB field, while sample 02GU12A is located not far from the EMII field.

#### Metamorphic rocks

**Granulite** The  $\epsilon_{\text{Nd}}$  value (+7.6) of the granulite falls in the range of OIB. In the  $\epsilon_{\text{Nd}}$  vs.  $(^{87}\text{Sr}/^{86}\text{Sr})_i$  correlation diagram (Fig. 4a), the granulite [ $(^{87}\text{Sr}/^{86}\text{Sr})_i = 0.70386$ ] plots to the right of the mantle array, towards the high  $(^{87}\text{Sr}/^{86}\text{Sr})_i$  ratios. In the  $(^{208}\text{Pb}/^{204}\text{Pb})_i$ – $(^{206}\text{Pb}/^{204}\text{Pb})_i$  diagram this rock plots above the NHR line, not far from the field of the Ecuadorian Late Cretaceous oceanic plateau accreted fragments (Fig. 4b). In the  $(^{207}\text{Pb}/^{204}\text{Pb})_i$  and  $\epsilon_{\text{Nd}}$  vs.  $(^{206}\text{Pb}/^{204}\text{Pb})_i$  diagrams, the granulite plots between the MORB and EMII areas (Figs. 4c and 4d).

**Amphibolites** Three amphibolites out of four have high  $\epsilon_{\text{Nd}}$  values of +4.9 and +7.9 while sample 03SQ9 differs by a low  $\epsilon_{\text{Nd}}$  value of +2 (Table 5). The amphibolites with high  $\epsilon_{\text{Nd}}$  values (02GU6, 03G23, 04SQ3) fall in the range of the Caribbean oceanic plateau basalts (Kerr *et al.*, 2002). Their  $(^{87}\text{Sr}/^{86}\text{Sr})_i$  ratios are less homogeneous than the Nd isotopic compositions and range between 0.703534 and 0.703926. The Pb isotopic ratios do not vary significantly. In the  $\epsilon_{\text{Nd}}$ – $(^{87}\text{Sr}/^{86}\text{Sr})_i$  diagram (Fig. 4a), only one sample out of four plot on the mantle array. The two remaining rocks are located on the right side of the diagram, towards the high  $(^{87}\text{Sr}/^{86}\text{Sr})_i$  values. In the  $(^{208}\text{Pb}/^{204}\text{Pb})_i$  vs.  $(^{206}\text{Pb}/^{204}\text{Pb})_i$  plot (Fig. 4b), the amphibolites cluster in the field of the accreted late Cretaceous oceanic plateau rocks (Mamberti *et al.*, 2003, 2004). In the  $(^{207}\text{Pb}/^{204}\text{Pb})_i$  and  $\epsilon_{\text{Nd}}$  vs.  $(^{206}\text{Pb}/^{204}\text{Pb})_i$  correlation diagrams, the amphibolites plot between MORB and EMII fields (Figs. 4c and 4d).

**Banded amphibolites** The  $\epsilon_{\text{Nd}}$  values of the banded amphibolites range from +6.5 to +1.8, and are similar to those of the non-banded amphibolites (Table 5). The  $(^{87}\text{Sr}/^{86}\text{Sr})_i$  of sample 03G22B falls in the range of amphibolite and granulite (Fig. 4a). In the  $(^{208}\text{Pb}/^{204}\text{Pb})_i$  and  $(^{207}\text{Pb}/^{204}\text{Pb})_i$  vs.  $(^{206}\text{Pb}/^{204}\text{Pb})_i$  correlation diagrams (Figs. 4b and 4c), sample 03G22B plots in the EMII and accreted Late Cretaceous oceanic plateau rocks fields, respectively. Because of its rather low  $\epsilon_{\text{Nd}}$  value (+2), this sample plots between the BSE and EMII fields in the  $\epsilon_{\text{Nd}}$ – $(^{206}\text{Pb}/^{204}\text{Pb})_i$  diagram (Fig. 4d).

**Micaschists** The  $(^{87}\text{Sr}/^{86}\text{Sr})_i$  of sample 04SJ1 falls in the range of the crustal sediments (Fig. 4a). In the  $(^{208}\text{Pb}/^{204}\text{Pb})_i$  and  $(^{207}\text{Pb}/^{204}\text{Pb})_i$  vs.  $(^{206}\text{Pb}/^{204}\text{Pb})_i$  correlation diagrams (Figs. 4b and 4c) they fall in the lower continental crust range. In the  $\epsilon_{\text{Nd}}$ – $(^{206}\text{Pb}/^{204}\text{Pb})_i$  diagram the samples fall between MORB and EMII (Fig. 4d).

#### Melagabbronorites and ultramafic rocks

##### Melagabbronorites and pyroxenites

Melagabbronorites and pyroxenites have quite similar  $\epsilon_{\text{Nd}}$  values of +6.5 and +7.0 respectively (Table 5). Samples 03SJ4 (melagabbronorite) and 04SQ11 (pyroxenite) have homogeneous  $(^{87}\text{Sr}/^{86}\text{Sr})_i$  isotopic compositions, with ratios of 0.703535 and 0.703553 respectively. In the  $\epsilon_{\text{Nd}}$ – $(^{87}\text{Sr}/^{86}\text{Sr})_i$  diagram (Fig. 4a), the samples are located on the right side of the diagram. In the  $(^{208}\text{Pb}/^{204}\text{Pb})_i$  vs.  $(^{206}\text{Pb}/^{204}\text{Pb})_i$  plot (Fig. 4b), the pyroxenites cluster in the field of the late Cretaceous accreted oceanic plateau rocks (Mamberti *et al.*, 2003, 2004).

In the  $(^{207}\text{Pb}/^{204}\text{Pb})_i$  vs.  $(^{206}\text{Pb}/^{204}\text{Pb})_i$  correlation diagram, the melagabbronorite sample 03G18 plots in the EMII field. The foliated pyroxenites plot in the MORB field (Fig. 4c). In the  $\epsilon_{\text{Nd}}$  vs.  $(^{206}\text{Pb}/^{204}\text{Pb})_i$ , the pyroxene-rich rocks plot between MORB and EMII fields (Fig. 4d).

**Peridotites and harzburgite** Due to their extremely low concentration of Pb, Sr and Nd, no isotopic data have been obtained for both peridotites and harzburgite

## DISCUSSION

### Protolith and genesis of deep rocks of Western Cordillera of Ecuador

#### Protolith of the mafic granulite and amphibolites

The mafic granulite major element composition is similar to that of MgO-rich basalts studied in the Ontong Java plateau (Kroenke-type basalt, Fitton and Godard, 2004). Considering trace element values, i.e., flat REE and multi-element patterns, the mafic granulite exhibits affinity with oceanic plateau basalts (OPB). It differs, however, from the Mg-rich basalts and ankaramites exposed in the Western Cordillera of Ecuador, considered as accreted remnants of the Cretaceous Caribbean–Colombian plateau (Kerr *et al.*, 2002; Mamberti *et al.*, 2003; Kerr and Mahoney, 2007), since the latter are enriched in LREE. Nevertheless, the  $\epsilon_{\text{Nd}}$  value (+7.6) of the mafic granulite plots in the fields of both the OPB and Mg-rich basalts and ankaramites. However, the Pb isotopic composition of this mafic metamorphic rock differs significantly from those of the Ecuadorian Mg-rich basalts and ankaramites, especially for  $(^{206}\text{Pb}/^{204}\text{Pb})_i$  which is significantly higher in the ankaramites ( $(^{206}\text{Pb}/^{204}\text{Pb})_i = 19.6$ ) (Mamberti *et al.*, 2004).

The amphibolites resemble the OPB in their similar major and trace elements, and Nd isotopic compositions (Fig. 4). However, they differ from the Ecuadorian accreted plateau basalts by having higher  $(^{207}\text{Pb}/^{204}\text{Pb})_i$  initial ratios. Surprisingly, in the  $(^{207}\text{Pb}/^{204}\text{Pb})_i$ – $(^{206}\text{Pb}/^{204}\text{Pb})_i$  diagram, the amphibolites and mafic granulites fall in the field of the Late Cretaceous intra-oceanic arc (Chiaradia and Fontboté, 2002; Allibon *et al.*, 2005).

Therefore, the mafic granulite and amphibolites likely

represent remnants of metamorphosed oceanic plateau basalts, accreted to the Pacific margin of Ecuador during the Late Cretaceous and/or the Paleogene, and exhumed along the Miocene strike-slip faults. The high  $(^{207}\text{Pb}/^{204}\text{Pb})_i$  ratios of the metamorphic rocks could be explained by the contribution of sediments, an interpretation consistent with the slightly higher  $^{87}\text{Sr}/^{86}\text{Sr}$  ratios of these samples, relatively to others. Amphibolite sample 03SQ9 exhibits a very low  $\epsilon_{\text{Nd}}$  value, which could be attributed to a higher slab component contribution. The metamorphism that has affected these rocks could have occurred during the intra-oceanic subduction, leading to the development of the Late Cretaceous arcs before their accretion to the Ecuadorian margin. This interpretation is similar to that of Weber *et al.* (2002), who studied xenolites from late Cenozoic volcanics from southwestern Colombia. These authors suggested that the lower crust in the Northern Volcanic Zone is basaltic in composition, and that it has been metamorphosed under amphibolite- or granulite-facies conditions by subduction processes.

#### *Protolith of the banded amphibolites*

The banded amphibolites have high contents of MgO (13 to 19%), CaO (12%) and  $\text{Al}_2\text{O}_3$  (12 to 15%), and exhibit  $\text{TiO}_2$  content (0.12 to 2%) lower than those commonly measured for basalts (Table 3). The multi-element plots are characterized by positive Eu and Sr anomalies reflecting plagioclase accumulation. The REE patterns of the banded amphibolites are LREE-depleted, and broadly similar to those of clinopyroxene. Thus, the protoliths of the banded amphibolites are likely clinopyroxene-rich gabbroic cumulates. This is also evidenced by the Ca-rich ( $\text{An}_{85}$ ) composition of the plagioclase and the high Mg content ( $\text{MgO} > 13\%$ ) of the metamorphic amphibole.

A question arises then: to which accreted unit belong these clinopyroxene-bearing gabbros? Compared to the San Juan clinopyroxene cumulate gabbros, the banded amphibolites differ by their major element compositions and REE patterns (Lapierre *et al.*, 2000; Mamberti *et al.*, 2003). The amphibolites have  $\text{SiO}_2$  between 47 to 58%, while the San Juan clinopyroxene gabbros have  $\text{SiO}_2$  contents lower than 49% (with the exception of an amphibole-bearing gabbro). The banded amphibolites are systematically depleted in LREE, while the San Juan clinopyroxene gabbros have flat to slightly LREE-depleted patterns. With the exception of one sample (03G22B) with a low  $\epsilon_{\text{Nd}}$  (+1.8), the banded amphibolites are characterized by a limited range of  $\epsilon_{\text{Nd}}$  (+5 to +6.5) that fall in the field of the San Juan mafic cumulates ( $\epsilon_{\text{Nd}}$  ranges between +8.1 and +5.2). However, alike the amphibolites, the banded amphibolites differ from the oceanic plateau cumulates by presenting higher Pb initial ratios, in particular the  $(^{207}\text{Pb}/^{204}\text{Pb})_i$  ratios.

It is well known that during their ascent to the sur-

face, intra-oceanic arc magmas can be trapped in oceanic crust in magma chambers and thus form cumulates. Such gabbroic cumulates have been described at the base of the Bonanza arc exposed on Vancouver Island (Western Canada, DeBari *et al.*, 1999) and have been recognized, by some authors in the Kohistan arc (Jijal Complex, Jan and Howie, 1981; Chilas Complex, Bard, 1983). Bonanza arc-cumulate gabbros (gabbro–norite) consist of Ca-rich plagioclase, clinopyroxene, orthopyroxene and Fe–Ti oxides when they are exposed in the lower crustal levels, while amphibole occurs in the mineralogy when they crystallized in higher crustal levels. The whole-rock major element chemistry is variable and depends on the modal percentage of the mineral composition (pyroxenes vs. plagioclase). However,  $\text{TiO}_2$  is low and less than 1%. The Bonanza gabbro–norites show positive Eu and Sr anomalies and are noticeably LREE-depleted. These features are due to clinopyroxene and plagioclase accumulation. The primitive mantle- or N-MORB normalized-multi-element patterns of the Bonanza and Chilas arc-derived gabbros are characterized by significant negative Nb and Ta anomalies. This comparison suggests that the studied banded amphibolites derive from intra-oceanic magmatic arc cumulates formed in lower crustal levels.

#### *Protolith of gabbros*

Among the unmetamorphosed cumulate gabbros, the mineralogy and compositional characteristics of samples 02GU12A, 03G21 are very similar to those of the Bonanza arc gabbro–norites and amphibole-bearing gneisses.

On the basis of Nd isotopes, two groups of rocks can be recognized among the unmetamorphosed and metamorphosed arc-cumulate gabbros of the Western Cordillera. The first group consists of samples 02GU12A, 03G21, 04GU8, 04GU12, and is characterized by high positive  $\epsilon_{\text{Nd}}$  values (+6.5 to +8.8). The second group includes sample 03G22B, and differs from group 1 by lower  $\epsilon_{\text{Nd}}$  values (+1.8). The high positive  $\epsilon_{\text{Nd}}$  values of group 1 suggest that the metamorphosed and unmetamorphosed cumulate arc-gabbros were derived from a depleted mantle source, devoid of any continental crust contamination. The  $\epsilon_{\text{Nd}}$  values of group 1 are similar to those of the Ecuadorian Late Cretaceous intra-oceanic arcs. Thus, group 1 cumulate arc-gabbros could represent the lower crustal levels of the Late Cretaceous intra-oceanic arcs. The low  $\epsilon_{\text{Nd}}$  values of sample 03G22B, suggest that continental crust material is involved in the genesis of these rocks.

#### *Protolith of micaschists*

The micaschists are similar to those of the Raspas Metamorphic Complex exposed in SW Ecuador (Fig. 1, Bosch *et al.*, 2002). The paragenesis of the meta-sediments (Table 1) corresponds to clay-rich sedimentary rocks metamorphosed in HP-BT conditions, most probably in a subduction zone. These meta-sediments are characterized by LREE-, Rb, Nb, U, Th, and Pb enrichments,

and by negative Eu anomaly. The isotopic data (low  $\epsilon_{Nd}$  value combined with high Pb and Sr isotopic signatures) suggest that the sediments derived from erosion of old continental crust.

#### *Genesis of melagabbonorites and pyroxenites*

The pyroxene-rich rocks show either cumulate textures (melagabbonorites) or foliated textures (pyroxenites). The foliated pyroxenites include green Al-rich spinel, absent in cumulates. This difference should be related to higher temperature (and pressure) conditions for crystallization of the foliated pyroxenites. The Al-rich phase is plagioclase in the melagabbonorites, and spinel in the foliated pyroxenites.

Like the cumulate gabbros and the banded amphibolites, the melagabbonorites likely belong to the lower crustal levels of the late Cretaceous arcs. Their mineralogy is very similar to the pyroxenites of the Jurassic Bonanza arc. Like the latter, the Ecuadorian melagabbonorites consist of Mg-rich clinopyroxene (diopside), Mg-rich orthopyroxene (En<sub>90-80</sub>) with locally Mg-rich olivine (Fo<sub>80</sub>) and Ca-plagioclase (An<sub>90</sub>). Thus, the modal mineralogy, bulk composition and textures of the gabbros and melagabbonorites suggest accumulation of magnesian pyroxene. The trace element chemistry of the pyroxenites is dominated by the clinopyroxene, i.e., LREE-depleted patterns, and very low contents in incompatible elements (U, Th, Nb and Ta). The positive Sr and Eu anomalies of the melagabbonorites are attributed to the presence of plagioclase.

The trace element patterns show marked negative Nb and Ta anomalies. The percentages of Al<sub>2</sub>O<sub>3</sub> and Mg# of clinopyroxenes (% Al<sub>2</sub>O<sub>3</sub> = 1–3.6 and Mg# = 0.84–0.88) and orthopyroxenes (% Al<sub>2</sub>O<sub>3</sub> = 1.8–2.2 and Mg# = 0.84) are characteristic of the crustal-arc pyroxene field (Parkinson and Pearce, 1998). Isotopic compositions show that the melagabbonorites share with the cumulate gabbros and banded amphibolites similar and homogeneous  $\epsilon_{Nd}$  values (+6.7 and +7). Reported in the <sup>207</sup>Pb/<sup>204</sup>Pb vs. <sup>206</sup>Pb/<sup>204</sup>Pb diagram, the melagabbonorites show the influence of an EMII component. This can be related to an arc environment.

The foliated pyroxenites 03SQ22 and 04SQ11 show geochemical features close to those of the pyroxenites from the Solomon Island (Santa Isabel and San Jorge pyroxenites; Berly *et al.*, 2006). The pyroxenites possess a LREE-depleted pattern. The rare earth element patterns show negative Nb and Ta anomalies and positive Sr anomalies. The percentage of Al<sub>2</sub>O<sub>3</sub> and Mg# of clinopyroxenes (% Al<sub>2</sub>O<sub>3</sub> = 4.2–8.5 and Mg# = 0.9–0.93) and orthopyroxene (% Al<sub>2</sub>O<sub>3</sub> = 4.5–6.2 and Mg# = 0.92) is in accordance with those of mantle pyroxenites (Wilkinson and Stolz, 1997; Garrido and Bodinier, 1999; Zanetti *et al.*, 1999; McInnes *et al.*, 2001). The Pb, Sr and Nd isotopic compositions of foliated pyroxenites are

similar to MORB.

Various hypotheses can be proposed to explain the formation of pyroxenites. One hypothesis proposes that the pyroxenites can be formed by melt/fluid rock reaction occurring in the upper mantle (McInnes *et al.*, 2001; Wang *et al.*, 2001). For example, the formation of the pyroxenites from Solomon Islands is explained by interaction between an aqueous fluid and a harzburgitic upper mantle component (Berly *et al.*, 2006). Similarly, the foliated pyroxenites of Ecuador could originate from a depleted mantle contaminated by fluids active in the mantle wedge during subduction processes.

#### *Genesis of lherzolites and harzburgite*

The petrography (Table 1) and trace elements features (Nb–Ta negative anomalies) of the lherzolites and harzburgite suggest that they were derived from a depleted mantle contaminated by slab-derived fluids during subduction processes. Their granoblastic texture attests to the equilibrium conditions during crystallization. The elongated and deformed minerals are correlated to plastic deformation conditions. The harzburgite differs from the lherzolites by its lower REE concentration and by its U-shaped REE pattern (Fig. 3E). Although the U-shaped REE distribution is still debated (Bodinier and Godard, 2003), we propose that this feature results from the addition of subduction fluid to highly depleted mantle peridotite. The presence of clinopyroxene in the lherzolite indicates either a more fertile peridotite or metasomatic enrichment; the presence of plagioclase indicates equilibrium at shallow level. The Nb–Ta and Sr anomalies provide evidence that these processes happened in a subduction setting.

## CONCLUSIONS

In the Western Cordillera of Ecuador, mafic igneous rocks (basalts, gabbros), ultramafic deformed rocks, metamorphic rocks and sedimentary rocks were exhumed during the Miocene along a transpressive dextral shear zone. The metamorphic rocks are granulites, amphibolites and garnet-bearing metasediments. The mafic igneous and metamorphic rocks exhibit oceanic plateau or arc affinities, and represent remnants of oceanic plateaux and associated arcs. The mafic high-grade metamorphic rocks result from intra-oceanic HT-LP metamorphism, probably related to the Caribbean plume event. The ultramafic rocks represent fragments of depleted mantle, deformed cpx-rich cumulate and continental lithospheric mantle or subduction-fluid contaminated mantle. The sedimentary rocks are either micaschists metamorphosed under HP-LT conditions, most probably in a subduction zone, or pelagic radiolarian cherts. Therefore, all these rocks are remnants of oceanic terranes that accreted to the Ecuadorian margin between ~80 and 40 Ma.

We can assume that the transpressive fault system randomly sampled these rocks at depth, although very deep rocks have not been sampled. As a matter of fact, the high grade metamorphic rocks most probably result from a Cretaceous intra-oceanic HT metamorphism (Beaudon *et al.*, 2005; Vallejo *et al.*, 2006), which seems to be not affected by more HT metamorphism, related to the Tertiary to recent magmatic arc activity in the Western Cordillera. However, since many of these samples come from deep levels of the oceanic crust and because we did not find remnants of continental material, we propose that the Western Cordillera is constituted at depth by oceanic material tectonically underplated during the accretion processes. This implies that the oceanic material was not obducted upon the continental crust during its accretion, and was rather tectonically underplated below, or accreted aside, the continental margin. Whatever the case, this suggests that the Western Cordillera of Ecuador is supported by a crustal root made of oceanic material.

**Acknowledgments**—This work was supported by funding from the Dyeti CNRS program and from the French Institut de Recherche pour le Développement (IRD). We are indebted to Catherine Chauvel Nick Arndt (Grenoble) for her help in the final version of this work. Many thanks go to Sylvain Campillo for his help during laboratory work and to Pierre Brunet for analytical assistance during TIMS in Toulouse. We also thank Anne de Vernal, Alain Tremblay, Michel Jébrak and Michelle Laithier of University of Quebec in Montreal (UQAM). Discussions with Matthias Bernet and Philippe Pagé were important to improve style and content. We are particularly grateful to the handling editor Michele Lustrino for his precious comments and help.

## REFERENCES

- Allibon, J., Monjoie, P., Lapierre, H., Jaillard, E., Bussy, F. and Bosch, D. (2005) High Mg basalts in the Western Cordillera of Ecuador. Evidence of plateau root melting during Late Cretaceous arc magmatism. *Proceedings of the 6th International Symposium on Andean Geodynamics*, 33–35.
- Allibon, J., Monjoie, P., Lapierre, H., Jaillard, E., Bussy, F. and Bosch, D. (2008) The contribution of the young Cretaceous Caribbean Oceanic plateau to the genesis of late Cretaceous arc magmatism in the Cordillera Occidental of Ecuador. *J. South Amer. Earth Sci.* **26**, 355–368.
- Amórtegui, V. A. E. (2008) Nature et évolution métamorphique des terrains océaniques en Equateur: conséquences possibles sur la genèse des magmas adakitiques. *Géologie Alpine, Mémoire hors série* **49**, 1–115.
- Aspden, J. A. and Litherland, M. (1992) The geology and Mesozoic collisional history of the Cordillera Real, Ecuador. *Tectonophysics* **205**, 187–204.
- Baby, P., Rochat, P., Mascle, G.-H. and Hérail, G. (1997) Neogene shortening contribution to crustal thickening in the back arc of the Central Andes. *Geology* **25**, 883–886.
- Bard, J. P. (1983) Metamorphism of an obducted island arc; example of the Kohistan sequence (Pakistan) in the Himalayan collided range. *Earth Planet. Sci. Lett.* **65**, 113–144.
- Barragán, R., Geist, D., Hall, L. and Kurz, M. (1998) Subduction control on the compositions of lavas from the Ecuadorian Andes. *Earth Planet. Sci. Lett.* **154**, 153–199.
- Barrat, J. A., Keller, F. and Amossé, J. (1996) Determination of rare earth elements in sixteen silicate reference samples by ICP-MS after Tm addition and ion exchange separation. *Geostand. Newsl.* **20**, 133–139.
- Beaudon, E., Martelat, J.-E., Amórtegui, A., Lapierre, H. and Jaillard, E. (2005) Métabasites de la Cordillère Occidentale d'Équateur: témoins d'une racine océanique sous les Andes d'Équateur. *Comptes Rendus Géosciences* **337**, 625–634.
- Berly, T., Hermann, J., Arculus, R. and Lapierre, H. (2006) Supra-subduction zone pyroxenites from San Jorge and Santa Isabel (Solomon Islands). *J. Petrol.* **47**, 1531–1555.
- Bodinier, J.-L. and Godard, M. (2003) Orogenic, ophiolitic and abyssal peridotites. *Treatise on Geochemistry* (Holland, H. D. and Turekian, K. K., eds.), **2.04**, 103–170, Elsevier.
- Bosch, D., Gabriele, P., Lapierre, H., Malfere, J.-L. and Jaillard, É. (2002) Geodynamic significance of the Raspas Metamorphic Complex (SW Ecuador). Geochemical and isotopic constraints. *Tectonophysics* **345**, 83–102.
- Bourdon, E., Eissen, J.-P., Gütscher, M.-A., Monzier, M., Hall, M.-L. and Cotten, J. (2003) Magmatic response to early aseismic ridge subduction. the Ecuadorian margin case (South America). *Earth Planet. Sci. Lett.* **205**, 123–138.
- Chauvel, C. and Blichert-Toft, J. (2001) A hafnium isotope and trace element perspective on melting of the depleted mantle. *Earth Planet. Sci. Lett.* **190**, 137–151.
- Chiaradia, M. and Fontboté, L. (2002) Lead isotope systematics of Late Cretaceous–Tertiary Andean arc magmas and associated ores between 8°N and 40°S. evidence for latitudinal mantle heterogeneity beneath the Andes. *Terra Nova* **14**, 337–342.
- Cosma, L., Lapierre, H., Jaillard, É., Laubacher, G., Bosch, D., Desmet, A., Mamberti, M. and Gabriele, P. (1998) Pétrographie et géochimie de la Cordillère Occidentale du Nord del'Équateur (0°30' S). Implications tectoniques. *Bulletin de la Société Géologique de France* **169**, 739–751.
- Cotten, J., Le Dez, A., Bau, M., Caroff, M., Maury, R., Dulski, P., Fourcade, S., Bohn, M. and Brousse, R. (1995) Origin of anomalous rare-earth element and yttrium enrichments in subaerially exposed basalts: evidence from French Polynesia. *Chem. Geol.* **119**, 115–138.
- DeBari, S., Anderson, R. and Mortensen, J. (1999) Correlation among lower to upper crustal components in an island arc. the Jurassic Bonanza arc, Vancouver Island, Canada. *Can. J. Earth Sci.* **36**, 1371–1413.
- Dewey, J. F. and Lamb, S. H. (1992) Active tectonics of the Andes. *Tectonophysics*, **205**, 79–95.
- Egüez, A. (1986) Évolution cénozoïque de la cordillère occidentale septentrionale d'Équateur (0°15S–1°10S). *Les minéralisations associées*, Université de Paris, 6, 116 pp. (in French).
- Fitton, J. G. and Godard, M. (2004) Origin and evolution of magmas on the Ontong Java Plateau, in Origin and evolution of the Ontong Java Plateau. *Geol. Soc. Spec. Publ.* **229**,

- 151–178.
- Gansser, A. (1973) Facts and theories on the Andes. *J. Geol. Soc. London* **129**, 93–131.
- Garrido, C. J. and Bodinier, J. L. (1999) Diversity of mafic rocks in the Ronda peridotite. Evidence for pervasive melt-rock reaction during heating of subcontinental lithosphere by upwelling asthenosphere. *J. Petrol.* **40**, 729–754.
- Goossens, P. J. and Roe, W. I. (1973) Chemical composition and age determination of tholeiitic rocks in the basic Cretaceous Complex, Ecuador. *Geol. Soc. Amer. Bull.* **84**, 1043–1052.
- Guillier, B., Chatelain, J. L., Jaillard, É., Yepes, H., Poupinet, G. and Fels, J. F. (2001) Evidence for present-day reactivations of Mesozoic–Paleogene sutures in Northern Ecuador (South America). *Geophys. Res. Lett.* **28**, 3749–3752.
- Hofmann, A. W. (1997) Mantle geochemistry: the message from oceanic volcanism. *Nature* **385**, 219–229.
- Hughes, R. A. and Pilatasig, L. F. (2002) Cretaceous and Tertiary terrane accretion in the Cordillera Occidental of the Andes of Ecuador. *Tectonophysics* **345**, 29–48.
- Jaillard, É., Caron, M., Dhondt, A., Ordoñez, M., Andrade, R., Bengtson, P., Bulot, L., Capetta, H., Dávila, C., Díaz, R., Huacho, J., Huamán, C., Jiménez, D., Jiménez, N., Lascano, M., Montenegro, J., Néraudeau, D., Rivadeneira, M., Toro, J., Villagómez, R. and Zambrano, I. (1997) *Síntesis estratigráfica y sedimentológica del Cretáceo y Paleógeno de la cuenca oriental del Ecuador*. Orstom-Petroproducción Publication, Quito, 164 pp.
- Jaillard, É., Hérail, G., Monfret, T., Diaz Martinez, E., Baby, P., Lavenue, A. and Dumont, J.-F. (2000) Tectonic evolution of the Andes of Ecuador, Peru, Bolivia and northernmost Chile. *Tectonic Evolution of South America* (Cordani, U. G. et al., eds.), 481–559, *31st Geological Congress*, Rio de Janeiro.
- Jaillard, É., Hérail, G., Monfret, T. and Wörner, G. (2002) Andean geodynamics: main issues and contributions from the 4th ISAG, Göttingen. *Tectonophysics* **242**, 1–15.
- Jaillard, É., Ordoñez, O., Suárez, J., Toro, J., Iza, D. and Lugo, W. (2004) Stratigraphy of the Late Cretaceous–Paleogene deposits of the Western Cordillera of Central Ecuador. Geodynamic implications. *J. South Amer. Earth Sci.* **17**, 49–58.
- Jaillard, É., Lapierre, H., Ordoñez, M., Toro Álava, J., Amórtegui, A. and Vanmelle, J. (2009) Accreted oceanic terranes in Ecuador: Southern edge of the Caribbean Plate? *Geological Society London, Special Publication* (James, K., Lorente, M. A. and Pindell, J., eds.), **328**, 467–483, doi:10.1144/SP328.19.
- Jan, Q. and Howie, R. A. (1981) Metamorphosed basic and ultrabasic rocks of the Jijal complex, Kohistan, NW Pakistan. *J. Petrol.* **22**, 85–126.
- Kehrer, W. and Van der Kaaden, G. (1979) Notes on the Geology of Ecuador with special reference to the Western Cordillera. *Geologisches Jahrbuch, B* **35**, 5–57.
- Kerr, A. C. (2003) Oceanic Plateaus. *Treatise on Geochemistry*, 537–565, Elsevier Publ.
- Kerr, A. C. and Mahoney, J. (2007) Oceanic plateaus: Problematic plumes, potential paradigms. *Chem. Geol.* **241**, 332–353.
- Kerr, A. C., Tarney, J., Marriner, G. F., Nivia, A. and Saunders, A. D. (1997) The Caribbean–Colombian Cretaceous igneous province. The internal anatomy of an oceanic plateau. Large Igneous Provinces. continental, oceanic and planetary flood volcanism. *AGU Geophys. Monogr.* **100**, 123–144.
- Kerr, A. C., Aspden, J., Tarney, J. and Pilatasig, L. (2002) The nature and provenance of accreted oceanic terranes in western Ecuador. geochemical and tectonic constraints. *J. Geol. Soc. London* **159**, 577–594.
- Lapierre, H., Dupuis, V., Mercier de Lépinay, B., Tardy, M., Ruiz, J., Maury, R. C., Hernandez, J. and Loubet, M. (1997) Is the Lower Duarte igneous complex (Hispanola) a remnant of the Caribbean plume-generated oceanic plateau? *J. Geology* **105**, 111–120.
- Lapierre, H., Bosch, D., Dupuis, V., Polvee, M., Maury, R. C., Hernandez, J., Monié, P., Yéghicheyan, D., Jaillard, É., Tardy, M., Mercier de Lépinay, B., Mamberti, M., Desmet, A., Keller, F. and Sénebier, F. (2000) Multiple Plume Events in the genesis of the peri-Caribbean Cretaceous Oceanic Plateau Province. *J. Geophys. Res.* **105**, 8403–8421.
- Leake, B. E., Wooley, A. R., Arps, C. E. S., Birch, W. D., Gilbert, M. C., Grice, J. D., Hawthorne, F. C., Kato, A., Kisch, H. J., Krivovichev, V. G., Linthout, K., Laird, J., Mandarino, J. A., Maresch, W. V., Nickel, E. H., Schumacher, J. C., Smith, D. C., Stephenson, N. C. N., Ungaretti, L., Whittaker, E. J. W. and Youzhi, G. (1997) Nomenclature of Amphiboles. Report of the subcommittee on Amphiboles of the international mineralogical association, Commission on new minerals and mineral names. *The Canadian Mineralogist* **35**, 219–246.
- Lebrat, M., Megard, F., Dupuy, C. and Dostal, J. (1987) Geochemistry and tectonic setting of pre-collision Cretaceous and Paleogene volcanic rocks of Ecuador. *Geol. Soc. Amer. Bull.* **99**, 569–578.
- Litherland, M., Zamora, A., Egúez, A., Aspden, J., Baez, N., Beate, B., Benítez, S., Jaillard, E. and Van Thournout, F. (1993) Mapa geológico de la República del Ecuador, escala 1:1,000,000. Geological Survey Publ., Keyworth, U.K.
- Litherland, M., Aspden, J. A. and Jemielita, R. A. (1994) The metamorphic belts of Ecuador. *British Geological Survey, Overseas Memoir.* **11**, 147 pp.
- Luzieux, L., Heller, F., Spikings, R., Vallejo, C. and Winkler, W. (2006) Origin and Cretaceous history of the coastal Ecuadorian forearc between 1°N and 3°S: paleomagnetic, radiometric and fossil evidence. *Earth Planet. Sci. Lett.* **249**, 400–414.
- Mamberti, M., Lapierre, H., Bosch, D., Ethien, R., Jaillard, É., Hernandez, J. and Polvé, M. (2003) Accreted fragments of the Late Cretaceous Caribbean–Colombian Plateau in Ecuador. *Lithos* **66**, 173–199.
- Mamberti, M., Lapierre, H., Bosch, D., Jaillard, É., Hernandez, J. and Polvé, M. (2004) The Early Cretaceous San Juan plutonic suite, Ecuador. a magma chamber in an Oceanic Plateau. *Can. J. Earth Sci.* **41**, 1237–1258.
- McCourt, W. J., Duque, P., Pilatasig, L. F. and Villagómez, R. (1998) Mapa geológico de la Cordillera Occidental del Ecuador entre 1°–2° S., escala 1/200.000. CODIGEM-Ministerio de Energía y Minas-BGS publications, Quito (in

- Spanish).
- McCulloch, W. J. and Wasserburg, G. J. (1978) Sm–Nd and Rb–Sr chronology of continental crust formation. *Science* **22**, 1003–1011.
- McInnes, B. I. A., Gregoire, M., Binns, R. A., Herzig, P. M. and Hannington, M. D. (2001) Hydrous metasomatism of the oceanic sub-arc mantle, Lihir, Papua New Guinea; petrology and geochemistry of fluid-metasomatised mantle wedge xenoliths. *Earth Planet. Sci. Lett.* **188**, 169–183.
- Morimoto, N., Fabres, J., Ferguson, A., Ginzburg, I., Ross, M., Steifert, F. and Zussman, J. (1988) Nomenclature of pyroxenes. *Bull. Mineral.* **111**, 535–550.
- Müller, J. P., Kley, J. and Jacobshagen, V. (2002) Structure and Cenozoic kinematics of the Eastern Cordillera, southern Bolivia (21°S). *Tectonics* **21**, 1037, doi:10.1029/2001TC001340.
- Parkinson, I. J. and Pearce, J. A. (1998) Peridotites from the Izu–Bonin–Mariana forearc (ODP leg 125). evidence for mantle melting and melt-mantle interaction in the supra-subduction zone setting. *J. Petrol.* **39**, 1577–1618.
- Reynaud, C., Jaillard, E., Lapierre, H., Mamberti, M. and Mascle, G.-H. (1999) Oceanic plateau and island arcs of Southwestern Ecuador. their place in the geodynamic evolution of northwestern South America. *Tectonophysics* **307**, 235–254.
- Ruiz, G., Seward, D. and Winkler, W. (2004) Detrital thermochronology—a new perspective on hinterland tectonics, an example from the Andean Amazon Basin, Ecuador. *Basin Res.* **16**, 413–430.
- Sharma, M. and Wasserburg, G. F. (1996) The neodymium isotopic composition and rare earth patterns in highly depleted ultramafic rocks. *Geochim. Cosmochim. Acta* **60**, 4537–4550.
- Spikings, R.-A., Winkler, W., Seward, D. and Handler, R. (2001) Along-strike variations in the thermal and tectonic response of the continental Ecuadorian Andes to the collision with heterogeneous oceanic crust. *Earth Planet. Sci. Lett.* **186**, 57–73.
- Suarez, G., Molnar, P. and Burchfield, B. C. (1983) Seismicity, fault-plane solutions, depth of faulting, and active tectonics of the Andes of Peru, Ecuador and Southern Colombia. *J. Geophys. Res.* **88**, 10403–10428.
- Sun, S. S. and McDonough, W. F. (1989) Chemical and isotopic systematics of ocean basalts; implications for the mantle compositions and processes. *Geol. Soc. Amer. Spec. Publ.* **42**, 313–345.
- Taylor, S. R. and McLennan, S. (1985) *The Continental Crust: Its Composition and Evolution*. Blackwell Scientific Publications, Oxford, 312 pp.
- Todt, W., Cliff, R. A., Hanser, A. and Hofmann, A. W. (1996) Evaluation of a <sup>202</sup>Pb–<sup>205</sup>Pb double spike for high precision lead isotope analysis. *Geophys. Monogr. Amer. Geophys. Union* **95**, 429–437.
- Vallejo, C., Spikings, R. A., Luzieux, L., Winkler, W., Chew, D. and Page, L. (2006) The early interaction between the Caribbean Plateau and the NW South American Plate. *Terra Nova* **18**, 264–269.
- Vanmelle, J., Vilema, W., Faure-Brac, B., Ordoñez, M., Lapierre, H., Jiménez, N., Jaillard, E. and García, M. (2008) Pre-collision evolution of the Piñón oceanic terrane of SW Ecuador: Stratigraphy and geochemistry of the <<Calentura Formation>>. *Bulletin de la Société géologique de France* **179**, 433–444.
- Wang, Z., Sun, S., Hou, Q. and Li, J. (2001) Effect of melt-rock interaction on geochemistry in the Kudi ophiolite (western Kunlun Mountains, northwestern China). implication for ophiolite origin. *Earth Planet. Sci. Lett.* **191**, 33–48.
- Weber, M., Tarney, J., Kempton, P. and Kent, R. (2002) Crustal make-up of the northern Andes. Evidence based on deep crustal xenolith suites, Mercaderes, SW Colombia. *Tectonophysics* **345**, 49–82.
- White, W. M., Albarède, F. and Telouk, P. (2000) High-precision analyses of Pb isotope ratios by multi-collector ICP-MS. *Chem. Geol.* **167**, 257–270.
- Wilkinson, J. F. G. and Stolz, A. J. (1997) Subcalcic Clinopyroxenites and associated ultramafic xenoliths in alkali basalt near Glenn Innes, northeastern New South Wales, Australia. *Contrib. Mineral. Petrol.* **127**, 272–290.
- Zanetti, A., Mazzucchelli, M., Rivalenti, G. and Vannucci, R. (1999) The Finero phlogopite–peridotite massif, an example of subduction-related metasomatism. *Contrib. Mineral. Petrol.* **134**, 107–122.